The Astrophysical Journal, 819:155 (21pp), 2016 March 10 doi:10.3847/0004-637X/819/2/155

THE NANOGRAV NINE-YEAR DATA SET: NOISE BUDGET FOR PULSAR ARRIVAL TIMES ON INTRADAY TIMESCALES

M. T. Lam[1], J. M. Cordes[1], S. Chatterjee[1], Z. Arzoumanian[2], K. Crowter[3], P. B. Demorest[4], T. Dolch[1,5], J. A. Ellis[6,18], R. D. Ferdman[7], E. F. Fonseca[3], M. E. Gonzalez[3,8], G. Jones[9], M. L. Jones[10], L. Levin[10,11], D. R. Madison[1,12], M. A. McLaughlin[10], D. J. Nice[13], T. T. Pennucci[9,14], S. M. Ransom[12], X. Siemens[15], I. H. Stairs[3,7], K. Stovall[16], J. K. Swiggum[10,15], and W. W. Zhu[3,17]

[1] Department of Astronomy and Cornell Center for Astrophysics and Planetary Science, Cornell University, Ithaca, NY 14853, USA; mlam@astro.cornell.edu
[2] Center for Research and Exploration in Space Science and Technology and X-Ray Astrophysics Laboratory, NASA Goddard Space Flight Center, Code 662, Greenbelt, MD 20771, USA
[3] Department of Physics and Astronomy, University of British Columbia, 6224 Agricultural Road, Vancouver, BC V6T 1Z1, Canada
[4] National Radio Astronomy Observatory, P.O. Box 0, Socorro, NM 87801, USA
[5] Department of Physics, Hillsdale College, 33 E. College Street, Hillsdale, MI 49242, USA
[6] Jet Propulsion Laboratory, California Institute of Technology, 4800 Oak Grove Dr. Pasadena CA 91109, USA
[7] McGill Space Institute, 3550 University, Montreal, Quebec H3A 2A7, Canada
[8] Department of Nuclear Medicine, Vancouver Coastal Health Authority, Vancouver, BC V5Z 1M9, Canada
[9] Department of Physics, Columbia University, 550 W. 120th St. New York, NY 10027, USA
[10] Department of Physics, West Virginia University, P.O. Box 6315, Morgantown, WV 26505, USA
[11] Jodrell Bank Centre for Astrophysics, School of Physics and Astronomy, The University of Manchester, Manchester M13 9PL, UK
[12] National Radio Astronomy Observatory, 520 Edgemont Road, Charlottesville, VA 22903, USA
[13] Department of Physics, Lafayette College, Easton, PA 18042, USA
[14] University of Virginia, Department of Astronomy, P.O. Box 400325, Charlottesville, VA 22904-4325, USA
[15] Center for Gravitation, Cosmology and Astrophysics, Department of Physics, University of Wisconsin-Milwaukee, P.O. Box 413, Milwaukee, WI 53201, USA
[16] Department of Physics and Astronomy, University of New Mexico, Albuquerque, NM 87131, USA
[17] Max-Planck-Institut für Radioastronomie, Auf dem Hügel 69, D-53121, Bonn, Germany
Received 2015 December 28; accepted 2016 February 6; published 2016 March 8

ABSTRACT

The use of pulsars as astrophysical clocks for gravitational wave (GW) experiments demands the highest possible timing precision. Pulse times of arrival (TOAs) are limited by stochastic processes that occur in the pulsar itself, along the line of sight through the interstellar medium, and in the measurement process. On timescales of seconds to hours, the TOA variance exceeds that from template-fitting errors due to additive noise. We assess contributions to the total variance from two additional effects: amplitude and phase jitter intrinsic to single pulses and changes in the interstellar impulse response from scattering. The three effects have different dependencies on time, frequency, and pulse signal-to-noise ratio. We use data on 37 pulsars from the North American Nanohertz Observatory for GWs to assess the individual contributions to the overall intraday noise budget for each pulsar. We detect jitter in 22 pulsars and estimate the average value of rms jitter in our pulsars to be $\sim$1% of pulse phase. We examine how jitter evolves as a function of frequency and find evidence for evolution. Finally, we compare our measurements with previous noise parameter estimates and discuss methods to improve GW detection pipelines.

Key words: gravitational waves – pulsars: general

1. INTRODUCTION

Pulsar timing is used for a variety of unique applications in astrophysics and fundamental physics. These include mass determinations of neutron stars (NSs) and their binary companions to contrain compact object formation mechanisms and equations-of-state (Demorest et al. 2010; Antoniadis 2013); precision tests of general relativity and other theories of gravity (Will 2014); limits on changes in fundamental constants (Lazaridis et al. 2009; Shao & Wex 2013; Zhu et al. 2015); and, especially recently, using arrays of pulsars as detectors of low-frequency (nanohertz) gravitational waves (GWs; e.g., Arzoumanian et al. 2015a, 2015c). Improvements in the accuracy of measured arrival times continue to yield benefits in these applications. In this paper, we present a detailed assessment of the time-of-arrival (TOA) noise budget that is applicable to measurements made on relatively short timescales, ranging from single pulse periods to integration times of 10–10^4 s. The work discussed here complements other studies that address noise contributions from variations in the spin rates of NSs (e.g., Hobbs et al. 2010; Shannon & Cordes 2010), the frequency dependence of pulse shapes (Pennucci et al. 2014), and from propagation through the interstellar medium (ISM; Armstrong 1984; Blandford et al. 1984; Foster & Cordes 1990; Rickett 1990; Cordes & Shannon 2010).

Pulsar timing relies on a foundation of pulsar phenomena that have been demonstrated over the nearly half century since pulsars were discovered (see Cordes 2013 for a review). Rotational stability, especially for recycled millisecond pulsars (MSPs), allows pulse arrival times to be predicted over long time scales so that small deviations from solar system and astrophysical effects can be determined (Verbiest et al. 2009). Radio emission beams appear to be locked to the crust of the NS and single pulses have phases that vary with respect to a fiducial phase that is also locked to the crust (Kramer et al. 1998; Cordes & Shannon 2010). Averages of N_p single pulses at a specific frequency converge to a stable pulse shape with fractional deviations $\sim 1/\sqrt{N_p}$, as expected for pulse fluctuations that are largely statistically independent (e.g., Dolch et al. 2014). While average pulse shapes do vary with

[18] Einstein Fellow.

frequency (Kramer et al. 1998), the pulse shapes of radio pulsars, including those objects having two or more stable shapes associated with metastable state of the magnetosphere (i.e., the shapes do not show evolution in time), are stable and show no secular evolution except for a few pulsars in NS–NS binaries where geodetic precession alters the orientation of the beam (Perera et al. 2010) and in the Crab pulsar in which large changes in pulse shape are seen over a few decades (Lyne et al. 2013). Magnetars also show secular changes in pulse shapes (e.g., Yan et al. 2015).

Intrinsic variations in pulses appear to have stationary statistics (Liu et al. 2011, 2012) in the same way that the average profile formed by averaging a large number of single pulses converges to a shape that appears to be epoch independent (see Craft 1970; Backer et al. 1975; Phillips & Wolszczan 1992; Hassall et al. 2012; Pilia et al. 2016). Consequently, pulse-to-pulse variations can be characterized for each pulsar and can be incorporated into timing studies that require a noise model, such as GW detection. Within a Bayesian framework, the average pulse profile and the pulse variations comprise some of the prior information that underlie modeling of pulsar orbits and GW detection (van Haasteren et al. 2009; Lentati et al. 2014).

In this paper, we focus on timescales smaller than one day and as short as a single spin period. Longer time spans require consideration of other phenomena, including pulsar spin variations and changes in the free-electron content along the line of sight. Intrinsic pulse variations comprise only one contribution to the arrival time variance on short timescales. A second contribution is the template-fitting error due to additive noise in the measured pulse shape which therefore, unlike single pulse variations, depends on the signal-to-noise ratio (S/N) of the average pulse (Cordes & Shannon 2010). A third contribution is due to changes in the interstellar impulse response from multipath scattering, which depends strongly on radio frequency (Cordes et al. 1990). The measured impulse response (or pulse broadening function, PBF) at a given time is caused by diffractive interstellar scattering/scintillation (DISS) and it varies as the finite number of constructive intensity maxima ("scintles") appearing in the measurement bandwidth changes. These white-noise contributions to arrival-time errors are referred to as pulse jitter, template-fitting errors, and scintillation noise, respectively. They have distinct correlations with time and frequency that can used to separate them empirically.

In Section 2, we describe the white-noise model. In Section 3, we briefly describe observations from the North American Nanohertz Observatory for GWs (NANOGrav) and the data sets used in our analysis. We discuss the analysis of individual objects in Section 4, discuss the collective results in Section 5, and analyze pulse jitter statistics in MSPs in Section 5.1. In Section 6 we compare our results with the parameterized Bayesian noise analysis reported in Arzoumanian et al. (2015b) and discuss the implications for pulsar timing array (PTA) optimization. We summarize our conclusions in Section 7.

2. MODEL FOR SHORT-TERM TIMING VARIANCE

We characterize the three white-noise contributions through appropriate analysis of short (~30 minutes) timing observations. Typical observing epochs are separated by several days or weeks, over which time each of the three contributions is uncorrelated, thus appearing as a white-noise perturbation of arrival times, $\Delta t(\nu, t)$. The total combined variance of the residuals[19] on short timescales is

$$\sigma_{\mathcal{R}}^2 = \sigma_{\rm S/N}^2 + \sigma_{\rm J}^2 + \sigma_{\rm DISS}^2, \quad (1)$$

where $\sigma_{\rm S/N}$ is the template-fitting error from a finite pulse S/N primarily due to radiometer noise, $\sigma_{\rm J}$ is the error due to pulse phase and amplitude jitter, and $\sigma_{\rm DISS}$ is due to scintillation noise. Spin noise, measurable over roughly yearly timescales, is negligible over a single epoch, as are changes in dispersion measure (DM $= \int dl\, n_{\rm e}$, the integral of the electron density over the line of sight) and in the mean shape of the PBF (see Appendix A for more details). For most objects we find $\sigma_{\rm S/N} > \sigma_{\rm J} \gg \sigma_{\rm DISS}$, while a few have $\sigma_{\rm J} \gtrsim \sigma_{\rm S/N}$ at some epochs of high S/N from periods of strong scintillation. Several objects show $\sigma_{\rm DISS}$ as the dominant timing error at particular radio frequencies (see Section 5).

In the following, we will consider the pulse shape model and individually discuss the TOA errors resulting from template fitting of finite S/N pulses, jitter, and scattering.

2.1. Pulse Shapes

Radio pulses are subject to a variety of perturbations as they travel between the pulsar and the Earth. To model the changes in pulse shape and intensity, we will assume that all chromatic delays have been perfectly removed or are negligible over each narrowband channel. These include the dispersive delay from DM, scattering, and frequency-dependent pulse profile evolution. We also assume that the signal polarization has been calibrated perfectly.

Under these assumptions, we model pulse shapes $I(\phi, \nu, t)$ as a function of phase ϕ obtained in short integrations longer than the pulse period, centered on time t and in a sub-band centered on frequency ν. The dominant remaining effect from scattering is the DISS intensity modulation associated with a small number of scintles in a time-frequency resolution cell. Refractive interstellar scintillation (RISS) will also modulate the signal strength but typically varies more slowly than DISS and is broadband (though still chromatic; Stinebring et al. 2000). It is assumed in the following discussion that we can resolve relevant pulse structure and scintillation fluctuations though in reality observing practices may not always allow for scintles to be fully resolved for a given pulsar. We also include a telescope bandpass function $H_{\rm tel}(\nu)$ that lumps together all frequency-dependent gains from the feed antenna to the output of the digital filterbank channel. The pulse shape model is then

$$\begin{aligned} I(\phi, \nu, t) = H_{\rm tel}(\nu)\{&g_{\rm RISS}(\nu, t) g_{\rm DISS}(\nu, t) \\ &\times [S_{\rm i}(\nu) p_{\rm i}(\phi, \nu, t)^* h_{\rm PBF}(\phi, \nu, t)] \\ &+ n(\phi, \nu, t)\} \end{aligned} \quad (2)$$

where $g_{\rm RISS}$ is the RISS modulation, $g_{\rm DISS}$ is the DISS modulation, $S_{\rm i}$ is the intrinsic spectrum of the pulsar, $p_{\rm i}$ is the intrinsic pulse shape normalized to unit area, $h_{\rm PBF}$ is the pulse broadening impulse response function, and n is additive radiometer noise. The intrinsic pulse shape is stochastic and includes contributions from phase and amplitude jitter. We

[19] Residuals ≡ (data−model), as discussed in Section 3. For the white-noise errors we consider, there is little difference between the pre- and-post-fit variance. The differences are discussed in Section 4 and Appendix A.

assume that the time-averaged intrinsic pulse shape, $\langle p_i(\phi, \nu, t)\rangle_t$, converges to a pulse template, $U(\phi, \nu)$, that is stable over long timescales. The template shape evolves as a slow function of frequency and the shape of each individual pulse is as well.

2.2. Template-fitting Errors

Template matching yields an rms error in the TOAs that depends on the S/N of the pulse. We assume for now that the data profile is a scaled and shifted version of the template with additive noise, the condition for matched filtering to yield the minimum possible TOA error (Turin 1960; Taylor 1992). This assumption breaks down when considering pulse phase jitter and the finite scintle effect, which change the profile dynamically and are discussed in the following subsections. Let $U(\phi)$ be the pulse template as a function of pulse phase ϕ normalized to unit amplitude, where we have dropped the explicit frequency dependence. The measured pulse intensity $I(\phi)$ at any epoch is then modeled as

$$I(\phi) = S\sigma_n U(\phi - \phi_0) + n(\phi), \tag{3}$$

where S is the S/N of the pulse profile (peak to off-pulse rms, written this way for clarity as a variable in equations), $n(\phi)$ is additive noise with rms amplitude σ_n, and ϕ_0 is the TOA. The TOA can be determined either through a cross-correlation analysis with proper interpolation of the cross-correlation function (CCF) to find the maximum or by least-squares fitting of the model template to the data. Mathematically, the two approaches are identical. The peak of the CCF of the template and pulse profile has an S/N related to S as (J. M. Cordes et al. 2016, in preparation)

$$S_{\rm CCF} = S\left[\sum_{i=0}^{N_\phi - 1} U^2(\phi_i)\right]^{1/2} \tag{4}$$

and is larger by a factor equal to the square root of the effective number of samples across the pulse if $n(\phi)$ is uncorrelated between phase bins. Template matching will fail when $S_{\rm CCF} \lesssim 1$.

For a pulse template with N_ϕ phase bins, the template-fitting error is (Cordes & Shannon 2010)

$$\sigma_{\rm S/N} = \frac{W_{\rm eff}}{S\sqrt{N_\phi}}, \tag{5}$$

where $W_{\rm eff}$ is an effective width[20] given by

$$W_{\rm eff} = \frac{P}{N_\phi^{1/2}\left[\sum_{i=1}^{N_\phi - 1}[U(\phi_i) - U(\phi_{i-1})]^2\right]^{1/2}} \tag{6}$$

for a pulsar with period P. We note that for Equation (5), if profiles are smoothed by n_s samples to increase $S \propto n_S^{1/2}$, the effective number of phase bins $N_\phi \propto n_s^{-1}$, leaving the product $N_\phi^{1/2}S$ invariant. The effective width is useful because it is unique to each pulsar-frequency combination and does not depend on any observational parameters. Therefore, it can be calculated using data obtained from one receiver-backend system and then the TOA error can be calculated for any value of S/N and number of phase bins. Any instrumental change, such as a change in $H_{\rm tel}(\nu)$ over time, that alters the pulse shape will have to be taken into account, however. The expression for $\sigma_{\rm S/N}$ yields the same value as the frequency-domain expression given by Taylor (1992).

2.2.1. The Role of DISS

The finite S/N causes the TOA to have a Gaussian error PDF under the assumption of the central limit theorem, $f_{\Delta t}(\Delta t|S) = \mathcal{N}(0, \sigma^2_{\rm S/N})$. DISS causes the S/N of the pulse to be modulated by a scintillation "gain," g. The gains have an exponential PDF $f_g(g) = \exp(-g)\Theta(g)$ where $\Theta(g)$ is the Heaviside step function (see Appendix B of Cordes & Chernoff 1997). Multiple scintillation maxima in the time-frequency plane will alter the PDF, which, given $n_{\rm ISS}$ scintles, is

$$f_g(g|n_{\rm ISS}) = \frac{(gn_{\rm ISS})^{n_{\rm ISS}}}{g\Gamma(n_{\rm ISS})}e^{-gn_{\rm ISS}}\Theta(g), \tag{7}$$

where Γ is the gamma function. When pulse shapes and TOAs are calculated, typically $n_{\rm ISS} \gtrsim 1$ scintles are averaged over the bandwidth and integration time, decreasing the variations in the scintillation gains.

We can transform the PDF of gains to the PDF of the observable pulse S/Ns with a change of variable to $g = S/S_0$, where S_0 is the mean S/N. The PDF is written as

$$f_S(S|n_{\rm ISS}) = \frac{(Sn_{\rm ISS}/S_0)^{n_{\rm ISS}}}{S\Gamma(n_{\rm ISS})}e^{-Sn_{\rm ISS}/S_0}\Theta(S). \tag{8}$$

As $n_{\rm ISS} \to \infty$, $f_S(S|n_{\rm ISS}) \to \delta(S - S_0)$, and the pulse S/N will be constant.

The PDF of the TOA errors is

$$f_{\Delta t}(\Delta t|n_{\rm ISS}) = \frac{1}{\sigma_{S_0}\sqrt{2\pi}}\left(\sqrt{2}\,n_{\rm ISS}\frac{\sigma_{S_0}}{|\Delta t|}\right)^{n_{\rm ISS}+1} \times H_{-(n_{\rm ISS}+1)}\left(\frac{n_{\rm ISS}\sigma_{S_0}}{\sqrt{2}\ |\Delta t|}\right) \tag{9}$$

where σ_{S_0} is the rms from template-fitting errors when no scintillation occurs (S is constant) and $H_n(x)$ is a Hermite polynomial of order n. See Appendix B for more details. In general, the distribution of measured S/N, $f_S(S)$, will be a convolution of several distributions, including the distribution of S/N intrinsic to the pulsar $f_{S_{\rm int}}(S)$, the DISS modulation $f_{S_{\rm DISS}}(S)$, and the RISS modulation $f_{S_{\rm RISS}}(S)$, which will also affect the distribution of TOA errors.

2.2.2. Example of a Single-component Gaussian Pulse

For a Gaussian pulse having width W (FWHM), the effective width (using Equation (6)) is

$$W_{\rm eff} = \frac{(WP)^{1/2}}{(2\pi \ln 2)^{1/4}}. \tag{10}$$

For this case, the effective width is proportional to the geometric mean of the period and actual pulse width. The

[20] This is a different definition than given in Cordes & Shannon (2010) although the rms error expressions are the same.

TOA error is

$$\sigma_{\rm S/N} = \frac{(WP)^{1/2}}{(2\pi \ln 2)^{1/4} N_\phi^{1/2} S} = \frac{W}{2(\ln 2)^{1/2} S_{\rm CCF}}, \quad (11)$$

where we have used Equation (4) to calculate

$$S_{\rm CCF} = \frac{S}{2}\left(\frac{2\pi}{\ln 2}\right)^{1/4}\left(\frac{WN_\phi}{P}\right)^{1/2} \approx 5.55\left[\left(\frac{W/P}{0.02}\right)\left(\frac{N_\phi}{2048}\right)\right]^{1/2} S. \quad (12)$$

The quantity W/P represents the fiducial duty cycle for an MSP. $S_{\rm CCF}$ must be of order unity or larger for template matching to fit appropriately.

2.3. Single Pulse Amplitude and Phase Variations ("Jitter")

Single pulses of both canonical pulsars and MSPs have been shown to have stochastic amplitude and phase variations (Cordes & Downs 1985; Cordes et al. 1990; Liu et al. 2012; Shannon & Cordes 2012; Dolch et al. 2014; Shannon et al. 2014). When averaged over $N_{\rm p}$ pulses to form a pulse profile, pulse jitter causes the underlying pulse shape to differ from that of the template, causing an error that is qualitatively different from additive noise. The jitter TOA error is independent of S/N. We define a dimensionless parameter $k_{\rm J} \equiv \sigma_{\rm J,1}/P$ as the ratio of rms phase variation of individual pulses $\sigma_{\rm J,1} = \sigma_{\rm J}\sqrt{N_{\rm p}}$ (in time units) to the period P of the pulsar. Cordes & Downs (1985) and Cordes & Shannon (2010) define a jitter parameter $f_{\rm J} = \sigma_{\rm J,1}/\sigma_U$, where σ_U is the equivalent rms width of the template. Since pulse profiles often display multiple components with potentially different jitter statistics, using $k_{\rm J}$ to compare the intrinsic jitter between pulsars is less dependent on the properties of the different components.

We note that single-component pulses that show phase variations only will have an rms jitter but those that show amplitude variations only will not display jitter. However, for pulses with multiple components, amplitude variations without phase variations will yield an rms jitter but only if the components overlap in pulse phase. An in-depth analysis on the role of multiple components in jitter will be presented in J. M. Cordes et al. (2016, in preparation). As an example, we consider a single component, Gaussian-shaped pulse with both a Gaussian phase jitter PDF with dimensionless phase variations $k_{\rm J,c}$ and amplitude variations with a modulation index $m_{\rm I,c}$ (defined as rms intensity divided by mean pulse amplitude). We use the subscript "c" to explicitly denote that the parameters describe the single component, whereas the parameter $k_{\rm J}$ is defined as the overall timing variation of the pulse. The TOA error is then (modified from the form in Cordes & Shannon 2010)

$$\sigma_{\rm J} = \frac{k_{\rm J} P}{\sqrt{N_{\rm p}}} = k_{\rm J,c} P\left(\frac{1 + m_{\rm I,c}^2}{N_{\rm p}}\right)^{1/2}. \quad (13)$$

Comparing the TOA errors from additive noise and jitter in Equations (5) and (13), we can define a transition S/N at which the two contributions are equal, $\sigma_{\rm S/N} = \sigma_{\rm J}$. The single-pulse S/N implied by a profile calculated from $N_{\rm p}$ pulses, assuming statistical independence of jitter between pulses, is $S_1 = N_{\rm p}^{-1/2} S$. For a Gaussian-shaped pulse, we find the single-pulse transition S/N, by setting Equations (11) and (13) equal when $N_{\rm p} = 1$, to be

$$S_{\rm 1,trans} = k_{\rm J,c}^{-1}\left(\frac{W}{P}\right)^{1/2}(2\pi \ln 2)^{-1/4}\left[N_\phi(1 + m_{\rm I,c}^2)\right]^{-1/2} \approx 0.216\left(\frac{k_{\rm J,c}}{0.007}\right)^{-1}\left(\frac{W/P}{0.02}\right)^{1/2} \times \left(\frac{N_\phi}{2048}\right)^{-1/2}\left(\frac{1 + m_{\rm I,c}^2}{2}\right)^{-1/2} \quad (14)$$

and the corresponding S/N of the CCF is

$$S_{\rm CCF1,trans} \approx 1.20\left(\frac{k_{\rm J,c}}{0.007}\right)^{-1} \times \left(\frac{W/P}{0.02}\right)\left(\frac{1 + m_{\rm I,c}^2}{2}\right)^{-1/2}, \quad (15)$$

where we set the fiducial $k_{\rm J} = k_{\rm J,c}(1 + m_{\rm I,c}^2)^{1/2} = 0.01$ based on our analysis in Section 5.1. When the single-pulse cross-correlation S/N is greater than about unity, the jitter error becomes larger than the template-fitting error.

The same pulsar-intrinsic effects that cause frequency-dependent template evolution will cause jitter to be a slow function of frequency as well. Over an observing band, we might approximate jitter as being frequency-independent (see Shannon et al. 2014 for evidence of decorrelation over widely separated frequencies) but frequency-dependence of the pulse template can be measurable (Dolch et al. 2014; Pennucci et al. 2014). We therefore note that jitter will be strongly correlated in frequency but not in time. DISS has a correlation bandwidth and timescale that can vary widely from pulsar to pulsar and between epochs for the same pulsar. Template-fitting errors are uncorrelated between time samples and frequency sub-bands.

2.4. Scintillation Timing Noise: Finite Scintle Effect

The time-frequency plane is made up of independent intensity fluctuations called scintles that are 100% modulated and have characteristic time and frequency scales $\Delta t_{\rm d}$ and $\Delta\nu_{\rm d}$, respectively. The scintillation structure is related to the temporal broadening of pulses, resulting in a time delay (Cordes et al. 1990; Cordes & Shannon 2010). Since a finite number of scintles will occupy the time–frequency plane, the instantaneous PBF will be different from the ensemble average shape. This produces an error that is statistically independent between two epochs and is therefore white noise in time.

The number of scintles for an observation of duration T and bandwidth B is approximately

$$n_{\rm ISS} \approx \left(1 + \eta_t \frac{T}{\Delta t_{\rm d}}\right)\left(1 + \eta_\nu \frac{B}{\Delta\nu_{\rm d}}\right). \quad (16)$$

The filling factors η_t, η_ν are less than unity and are in the range of 0.1–0.3 (Cordes & Shannon 2010; Levin et al. 2016), depending on the definitions of the characteristic timescale and bandwidth.

When $n_{\rm ISS}$ is large, the TOA error is

$$\sigma_{\rm DISS} \approx \frac{\tau_{\rm d}}{\sqrt{n_{\rm ISS}}} \quad (17)$$

where $\tau_{\rm d} = C_1/(2\pi\Delta\nu_{\rm d})$ is the scattering timescale with C_1 a coefficient of order unity. For a thin scattering screen with

uniscale irregularities, $C_1 = 1$ but for a Kolmogorov screen, $C_1 = 0.96$. For uniform, thick media, $C_1 = 1.53$ and 1.16, respectively, for uniscale and Kolmogorov media (Cordes & Rickett 1998). When there is only one scintle or a partial scintle across the band, the TOA error is approximately τ_d, or some fraction of it.

3. OBSERVATIONAL DATA

3.1. NANOGrav Timing Observations

We used pulse profile data from the NANOGrav nine-year data set described in Arzoumanian et al. (2015b, hereafter NG9) for our analysis. NG9 contains multi-frequency pulse profiles of thirty-seven MSPs observed at the Green Bank Telescope (GBT) and Arecibo Observatory (AO). Two generations of backends were used, the GASP/ASP backend earlier, processing up to 64 MHz (Demorest 2007; Demorest et al. 2013), and the GUPPI/PUPPI backends later, processing 100, 200, or 800 MHz of bandwidth (DuPlain et al. 2008; Ford et al. 2010). The larger bandwidth of GUPPI and PUPPI yields an increase in S/N from increased averaging of radiometer noise combined with a higher probability for large scintillation maxima (Pennucci et al. 2014). Because we wish to maintain homogeneity of the inferred parameters of our pulsars (e.g., consistent scintillation statistics), we analyze pulses observed with GUPPI/PUPPI only.

Each pulsar was observed at each epoch with at least two receivers. At GBT, the 820 and 1400 MHz bands were used, and at AO, the 430 and 1400 MHz or 1400 and 2300 MHz bands were used. PSRs B1937+21 and J1713+0747 were observed at both AO and GBT and we analyze both observatories' data sets independently to check for consistency across varying S/Ns. In addition, PSR J2317+1439 contained data from the 327 MHz band in addition to the 430 and 1400 MHz bands. We also used processed 430 MHz data available for PSRs B1937+21 and J2017+0603 though they were not included in NG9.

Pulse profiles were computed in real time by averaging together single pulses according to an initial timing model that includes the pulsar's spin kinematics and the orbital motions of the Earth and, if needed, the pulsar binary orbit. Model parameters were obtained by fitting to earlier observations. Raw data profiles from GUPPI/PUPPI were folded and de-dispersed in ∼10 s and ∼15 s subintegrations at AO and GBT, respectively, and every eight subintegrations were averaged together to reduce data volume through the NG9 pipeline. Some Arecibo 1400 MHz observations were initially recorded in ∼1 s subintegrations to aid in radio frequency interference (RFI) excision and then combined to form the ∼10 s "raw" subintegrations. Observations for a given epoch typically spanned about 0.5 hr. All profiles were divided into 2048 phase bins.

Arzoumanian et al. (2015b) describe the polarization calibration algorithm, as well as the RFI excision methods, for creating calibrated data profiles using the PSRCHIVE[21] software package (Hotan et al. 2004; van Straten et al. 2012). A broadband noise source was locally injected into the two polarization signal paths at each observatory prior to every pulsar observation and is recorded by the backend systems. Both differential gain and phase between the two hands of polarization were calibrated using the correlated noise source observation. The noise source power in each hand of polarization was not assumed to be equal and was measured separately roughly once per month per telescope per frequency by observing the noise source after pointing on and off a bright, unpolarized quasar. After balancing the gains of the two orthogonal polarizations, the intensity profiles were produced by summing the two polarization profiles. Future papers will discuss the complete polarization and flux calibration solutions at AO and GBT. Frequency channels known to consistently contain RFI signals were removed first. If the off-pulse variation in a 20-channel wide frequency window was four times the median variation value, those channels were also removed.

We took the calibrated profiles with ∼80 s (AO) and ∼120 s (GBT) subintegration lengths and average the profiles together into sub-bands of 50 MHz resolution. Frequency-averaging builds S/N for each pulse to avoid mis-estimation of the TOA in the low-S/N limit (see Appendix B of Arzoumanian et al. 2015b). We note that frequency-dependent profile shape changes across the entire observing band can be significant for some sources over the full band (e.g., see Pennucci et al. 2014) but are small over a 50 MHz channel.

We implemented a Fourier-domain TOA estimation algorithm (Taylor 1992) that determines the amplitude $S\sigma_n$, the TOA, and template-fitting uncertainty of an intensity profile $I(\phi, \nu, t)$. Template shapes $U(\phi)$ are determined from de-noised average profiles, smoothed by thresholding the coefficients of a wavelet decomposition of the pulse shape. One template is generated from all data for each pulsar, backend, and frequency band combination.[22] Timing offsets from profile frequency evolution are not accounted for here but will be accounted for in the analysis in the following section. We determined the off-pulse window for each pulse template used to measure σ_n by finding the rolling eighth (256 out of 2048 phase bins) of phase that has the smallest integrated intensity. The pulse baseline is defined as the mean of the off-pulse region and the noise σ_n is the rms amplitude of the region. Once we knew the best-fit amplitude and rms noise, we then calculated the associated S/N for each pulse. Our code is freely available in the PyPulse software package.[23]

3.2. Scintillation Parameters

Scintillation bandwidths and timescales were taken or estimated (using the scaling relations as a function of observing frequency in Cordes & Lazio 2002) from Keith et al. (2013) and Levin et al. (2016) and references therein. We used these measurements to derive values of $\sigma_{\rm DISS}$ given by Equation (17) assuming $\eta_\nu = \eta_t = 0.2$, $C_1 = 1$ (Lambert & Rickett 1999; Cordes & Shannon 2010; Levin et al. 2016), and integration time/bandwidth values equal to that of the profiles from each telescope. When scintillation parameters were not available, we estimated all other values using the NE2001 electron density model (Cordes & Lazio 2002).

[21] http://psrchive.sourceforge.net, accessed via scripts available at https://github.com/demorest/nanopipe.

[22] Templates are available in the NG9 data release at https://data.nanograv.org.

[23] https://github.com/mtlam/PyPulse

Table 1
Errors in Initial Timing Model

Effect	Typical Δt	Appendix Section	Comments
Pulse profile smearing			
Spin period error	$\lesssim$10 ps	A.1.1	systematic
Binary parameter errors	$\lesssim$10 ns	A.1.2	systematic
DM variations	$\lesssim$400 ns	A.1.3	stochastic
Polarization calibration gain errors	$\lesssim$1 μs	A.1.4	stochastic
Deviations from the polynomial fit			
Binary orbit parameter errors	$\lesssim$10 ps	A.2.1	systematic
Ionospheric DM variations	$\lesssim$1 ns	A.2.2	stochastic
Cross-coupling errors	?	A.2.3	systematic, highly pulsar-dependent
Rotation measure (RM) variations	$\lesssim$1 ps	A.2.4	stochastic
Spin noise	$\lesssim$0.1 fs	A.2.5	stochastic
Stochastic GW background	$\lesssim$1 fs	A.2.6	stochastic

4. SINGLE PULSAR ANALYSIS

We are interested in quantifying noise on intraday timescales. We therefore independently analyze individual NANOGrav observations, typically of duration 30 minutes or less. During an observation, the incoming data were folded using a pre-computed model pulsar ephemeris. We assumed that this ephemeris is sufficiently accurate that there is very little drift in pulse arrival times over an observation. We calculated pulse phases within an observation, "initial timing residuals" $\delta t(\nu, t)$, using the Fourier-domain estimation algorithm of Taylor (1992). We assumed that the initial timing model used for folding will yield polynomial expansions of phase and spin period that represent the state of the Earth–pulsar line of sight at a given epoch to high accuracy. We also assumed that the initial timing model is accurate such that pulse smearing will be negligible for our subintegration lengths. We then calculated "short-term" residuals $\mathcal{R}(\nu, t)$ over a single observation by fitting a polynomial model over all $\delta t(\nu, t)$ observed that includes a constant offset for TOAs from each frequency channel and a parabolic fit in time common to all TOAs. The initial and short-term models can be written as

$$\delta t(\nu, t) = K(\nu) + at + bt^2 + n(\nu, t) \quad (18)$$

$$\mathcal{R}(\nu, t) \equiv \hat{n}(\nu, t) = \delta t(\nu, t) - [\hat{K}(\nu) + \hat{a}t + \hat{b}t^2]. \quad (19)$$

Here, a and b are frequency-independent coefficients, $n(\nu, t)$ is additive noise in both time and frequency that includes the three white-noise components in Equation (1), and $K(\nu)$ represents a constant offset that varies with frequency, resulting from pulse profile evolution or epoch-dependent dispersion and scattering. Variables with carets denote estimated quantities. Thus, $\mathcal{R}(\nu, t)$ is the estimated additive noise, calculated by subtracting the estimated model parameters from the TOAs. We assumed that subtraction of the offsets removes any frequency-dependence between sub-bands. The variance removed by the fit for a, b, and $K(\nu)$ to obtain $\mathcal{R}(\nu, t)$ will be small for white-noise components that are uncorrelated in time.

Differences between the initial timing model and the short-term timing model for a given epoch can result from a number of possible effects that we account for with the quadratic fit in Equation (19). Table 1 lists the effects and their approximate amplitudes. We provide details of the estimates in Appendix A.

4.1. An In-depth Analysis of Jitter and Frequency-dependent Jitter Evolution in PSR J1713+0747

PSR J1713+0747 is not only one of the best-timed pulsars but it is the pulsar with the highest S/N pulses in our entire data set and is thus most sensitive to jitter error. The S/N peaked at $S \approx 2000$ at 1400 MHz for one of two observations on MJD 56380. Figure 1 shows the residuals of sub-bands for that observation in panel (a); strong correlation between sub-bands is evident and indicative of pulse jitter (Cordes & Shannon 2010; Shannon et al. 2014). Along with the ∼80 s data, we processed the ∼10 s subintegration raw data from this observation to demonstrate the lack of temporal correlation in the residuals, shown in panel (b), as expected when jitter noise becomes dominant. The results in Figure 1 are presented with the 80 s subintegrations displayed in the left panels and the 10 s subintegrations on the right.

Within each subintegration, we typically saw a monotonic increase or decrease in the residual with frequency, which is most evident in the second-to-last subintegration of the low-time-resolution residuals, highlighted with a black arrow in panel (a). Each line in panels (c) and (d) shows the residuals as a function of frequency for each subintegration. The subintegration highlighted with the arrow in panel (a) is marked with a thick, black line in panel (c) and demonstrates the trend increasing with frequency. We fit the slope of each line and plot the results in panels (e) and (f). The slope values show a deviation much larger than the median of the fitting errors, denoted by the dotted, horizontal lines. While the points in the time series in panel (e) appear correlated, they do not in panel (f), suggesting the slope changes are uncorrelated. The autocorrelation functions of the time series in panels (e) and (f) are shown in panels (g) and (h), respectively, and the flatness at non-zero lags demonstrates that the slope changes are consistent with uncorrelated, white noise in time.

The roughly monotonic slope of the residuals with frequency in each subintegration indicates that there is a systematic variation of the pulse shape for each subintegration (and thus TOAs) versus frequency, indicative of frequency-dependent jitter evolution, which is distinctly different from frequency-dependent pulse profile evolution, though related. These slopes are uncorrelated between subintegrations, indicating that longer averages of larger numbers of pulses will show less variation with frequency. Nonetheless, it is known that the average pulse

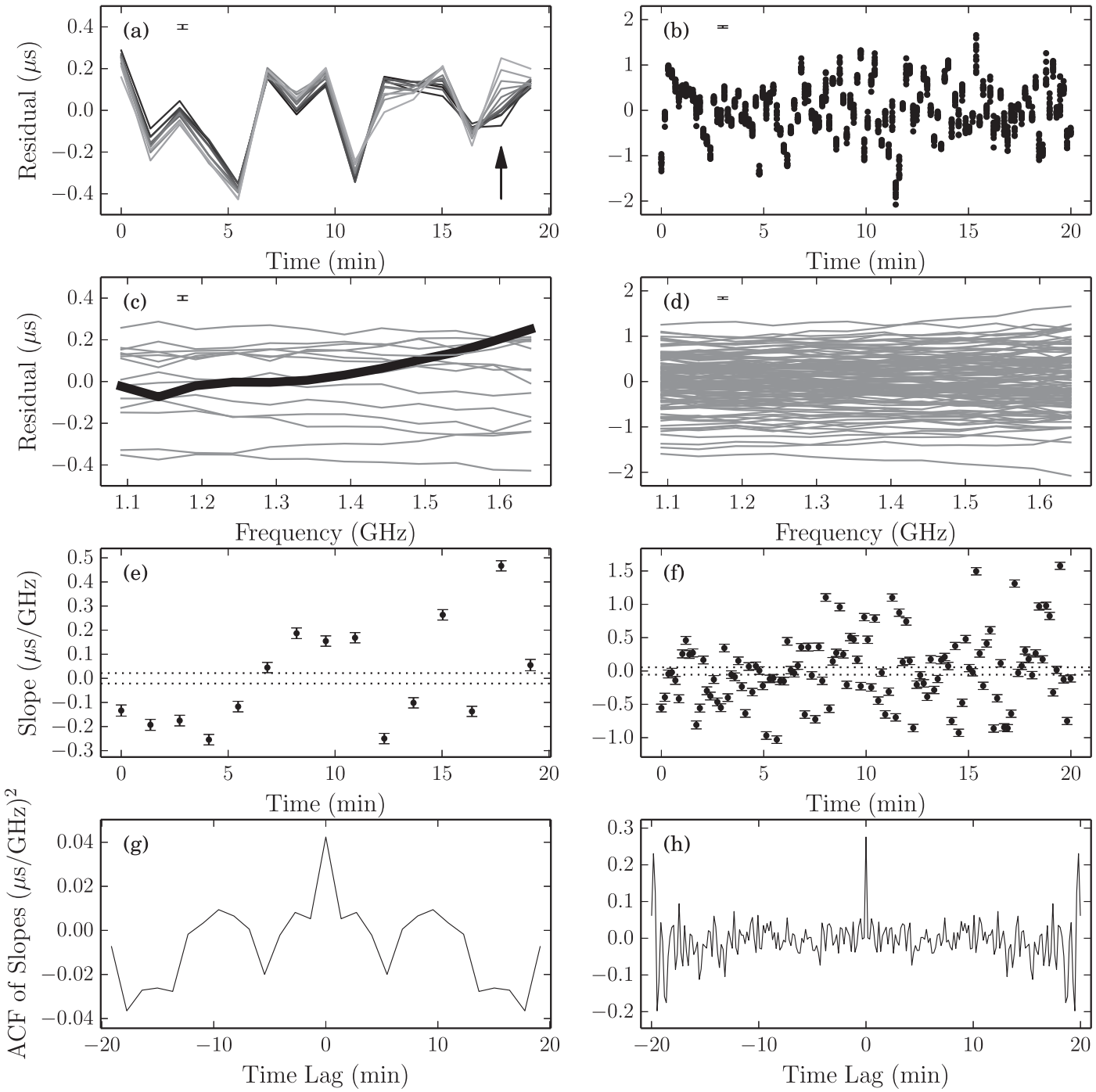

Figure 1. Analysis of jitter in residuals for the highest S/N epoch for PSR J1713+0747. The panels on the left side show the analysis for the ∼80 s subintegration data while the panels on the right side are for the ∼10 s subintegration data. Panel (a): low-time-resolution residuals as a function of time. Each frequency channel is shaded differently, with darker lines indicating lower frequencies. The arrow indicates the subintegration with the greatest change in residual vs. frequency. Typical TOA errors are shown in the top left of panels (a)–(d). Panel (b): high-time-resolution residuals as a function of time, where we have plotted residuals as points for clarity. Panels (c), (d): residuals as a function of frequency, where each line represents one subintegration. The thick, black line in panel (c) corresponds to the subintegration highlighted with the arrow in panel (a). Panels (e), (f): slopes of fitted lines to the residuals vs. frequencies for each subintegration. The horizontal, dotted lines indicate the median fitting error. Panels (g), (h): autocorrelation functions (ACFs) of the time series in panels (e) and (f), respectively.

shape of PSR J1714+0747 varies systematically with frequency (Dolch et al. 2014; Arzoumanian et al. 2015b) and those must reflect the variations occurring on the single-pulse level. For the high-time-resolution data, the rms slope is ≈0.53 μs GHz^{-1}.

4.2. Distributions of Residuals from Jitter and Scintillation

We modeled the variance in the residuals separately for each pulsar/backend/frequency band combination using Equation (1). While all three terms scale as $N_{\rm p}^{-1}$, only the

template-fitting term depends on the S/N of the pulse profile whereas the jitter and the DISS terms do not. Therefore, we used a one-parameter model for the variance as a function of S/N,

$$\sigma_{\mathcal{R}}^2(S) = \sigma_{\mathrm{S/N}}^2(S) + \sigma_{\mathrm{C}}^2 = \left(\frac{W_{\mathrm{eff}}}{S\sqrt{N_\phi}}\right)^2 + \sigma_{\mathrm{C}}^2. \quad (20)$$

where $\sigma_{\mathrm{C}}^2 = \sigma_{\mathrm{J}}^2 + \sigma_{\mathrm{DISS}}^2$, as implied by Equation (1), is the variance that is constant in S/N. At high S/N, $\sigma_{\mathrm{S/N}} \to 0$ and σ_{C}^2 becomes the dominant term. We took the scintillation parameters to be constant for all epochs so that σ_{DISS} is fixed, though measurements of these parameters indicate small variations (factor of $\lesssim$2) over many years, with some pulsar showing larger fluctuations (e.g., Coles et al. 2015).

The observed S/N PDF depends on the intrinsic pulse amplitude distribution, on modulations from DISS and RISS, and on variations of the system equivalent flux density (SEFD) of the receiver. We assumed that the average *intrinsic* flux density of the pulsar and SEFD were constant over all times. Therefore, the mean S/N, S_0, is constant for our many-period pulse averages (large N_{p}), i.e., $f_{S_0}(S) = \delta(S - S_0)$, assuming that changes in the S/N are due solely to modulation from DISS. RISS has been shown to change the observed flux density by a factor of $\lesssim$2 on the timescale of 10 s of days (Stinebring et al. 2000). Since we observed S/N variations spanning over an order of magnitude from the mean in some cases, we ignored the contribution to the S/N PDF from RISS.

We assumed that residuals at a given S/N follow a Gaussian distribution

$$f_{\mathcal{R}|S}(\mathcal{R}|S, \sigma_{\mathrm{C}}) = \frac{1}{\sqrt{2\pi\sigma_{\mathcal{R}}^2}} e^{-\mathcal{R}^2/(2\sigma_{\mathcal{R}}^2)}, \quad (21)$$

where again $\sigma_{\mathcal{R}}$ is a function of both S and σ_{C} (Equation (20)). The normality assumption is a good approximation due to the fact that while residuals must lie within one cycle of pulse phase, $|\mathcal{R}| \lesssim 0.001P$ and deviation from a Gaussian distribution is negligible. We removed all residuals with $S < 10^{0.5}$ ($\approx$3) to avoid contamination by low-significance noise being fit by the template matched filtering (see Appendix B of Arzoumanian et al. 2015b), which excluded five pulsar/backend/frequency band residual sets and two pulsars from our analysis entirely. We excised evident RFI beyond the methods described in Section 3 by inspection of the residuals and the corresponding pulse profiles.

We performed a maximum likelihood (ML) analysis over the residuals $\{S_{\mathrm{i}}, R_{\mathrm{i}}\}$ given the three parameters S_0, n_{ISS}, and σ_{C}. To include our cut in S/N, we included a parameter S_{min} and determined the factor that properly normalizes the distribution in S. The normalized distribution is

$$f_S(S|S_0, n_{\mathrm{ISS}}, S_{\mathrm{min}}) = f_s(S|S_0, n_{\mathrm{ISS}})\Theta(S - S_{\mathrm{min}}) \times \frac{\Gamma(n_{\mathrm{ISS}})}{\Gamma(n_{\mathrm{ISS}}, n_{\mathrm{ISS}}S_{\mathrm{min}}/S_0)}, \quad (22)$$

where $\Gamma(\alpha, x)$ is the incomplete Gamma function and $\Gamma(\alpha, 0) = \Gamma(\alpha)$ (see Equation (3.381.3-4) of Gradshteyn et al. 2007, for the relevant integrals).

The likelihood function can be calculated by combining Equations (7), (21), and (22),

$$\begin{aligned}\mathcal{L}(S_0, n_{\mathrm{ISS}}, \sigma_{\mathrm{C}}|\{S_i, R_i\}, S_{\mathrm{min}}) &= \prod_i f_{\mathcal{R},S}(\mathcal{R}_i, S_i|S_0, n_{\mathrm{ISS}}, \sigma_{\mathrm{C}}, S_{\mathrm{min}}) \\ &= \prod_i f_{\mathcal{R}|S}(\mathcal{R}_i|S_i, \sigma_{\mathrm{C}}) f_S(S_i|S_0, n_{\mathrm{ISS}}, S_{\mathrm{min}}), \end{aligned} \quad (23)$$

where i labels the individual residuals. We performed a grid search in the three-dimensional parameter space to estimate the values and uncertainties on the three model parameters. The likelihood function can be expressed as the product of individual likelihoods

$$\begin{aligned}&\mathcal{L}(S_0, n_{\mathrm{ISS}}, \sigma_{\mathrm{C}}|\mathcal{R}, S, S_{\mathrm{min}}) \\ &\quad = \mathcal{L}(\sigma_{\mathrm{C}}|\mathcal{R}, S, S_{\mathrm{min}})\mathcal{L}(S_0, n_{\mathrm{ISS}}|S, S_{\mathrm{min}}), \end{aligned} \quad (24)$$

so that we could perform the grid search in σ_{C} independently from the search in S_0, n_{ISS} space. We limited our search in n_{ISS} with a lower bound of 1 so that the minimum number of degrees of freedom across both the time and frequency dimensions is 2 (Cordes & Chernoff 1997), or that each pulse must come from at least one ray path through the ISM. An F-test was used to determine the significance of σ_{C} with a significance value of 0.05 (i.e., 2σ significant). If not, we computed the 95% upper limit on σ_{C}.

Figure 2 shows the results for one of NANOGrav's best-timed pulsars, PSR J1713+0747 observed at 1400 MHz at AO. The top panel shows the residuals $\mathcal{R}_{\mathrm{i}}(S_{\mathrm{i}})$ with the $\pm 3\sigma_{\mathcal{R}}$ ranges plotted in the blue lines. At higher S/N, the rms of the residuals asymptotes to a constant value, σ_{C}, represented by the constant width scatter of points, and is indicative of jitter and scintillation noise and the S/N regime over which they dominate the template-fitting error. A histogram of the residuals R_{i} are shown at right with bins $\Delta\mathcal{R} = 0.1$ μs and a histogram of S_{i} with logarithmic bins of $\Delta \log_{10} S = 0.0625$ is shown below with Poisson uncertainties shown by the error bars. We plot $Sf_S(S|S_0, n_{\mathrm{ISS}}, S_{\mathrm{min}})$ in the middle panel to properly compare the scaled PDF to the logarithmically binned histogram, with S_0 and n_{ISS} determined in the ML analysis.

The bottom panel shows the rms residual for the same logarithmic binning of the data. The dashed line shows the predicted rms from template-fitting error only given by Equation (5). We emphasize that the dashed line is not a fit to the data points in this plot. We see agreement between the dashed line and the points at low S/N for most pulsars, which indicates that Equation (5) represents the template-fitting noise well. Deviation from the line can be explained by other systematic effects that can increase the variance, such as remaining RFI in the data. The blue line shows the best estimate $\sigma_{\mathcal{R}}(S)$ from the ML analysis. We note that the ML analysis is less susceptible to parameter mis-estimation from the effects of RFI in the data over a fit of Equation (20) to the rms residual points because the ML analysis fits all of the data simultaneously.

Figures 3–6 show the same ML analysis for four other pulsars observed at 1400 MHz. While $\sigma_{\mathcal{R}}$ matches the data for PSR J1909−3744, the S/N histogram does not match well with the data and the PDF of n_{ISS} in the ML analysis peaks at the edge of the sampling space ($n_{\mathrm{ISS}} = 1$), expected since $\Delta\nu_{\mathrm{d}} = 39 \pm 14.7$ MHz and $\Delta t_{\mathrm{d}} = 2258$ s for the pulsar at a reference frequency of 1500 MHz (Keith et al. 2013; Levin

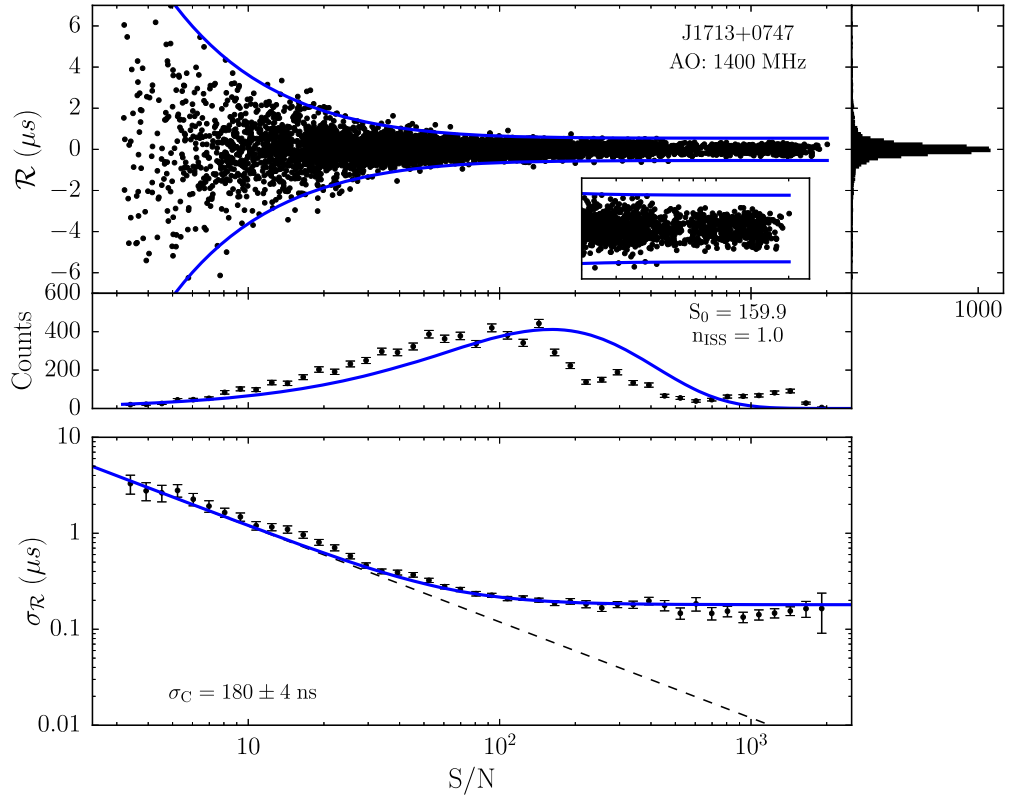

Figure 2. Analysis of residuals for PSR J1713+0747 observed at 1400 MHz with AO, containing the highest S/N residuals in our sample. Top: residuals $\mathcal{R}$ vs. S/N. The solid lines (blue) show the $\pm 3\sigma_{\mathcal{R}}(S)$ ranges from the maximum likelihood analysis. The inset shows the residuals for S/N greater than 70% of the maximum. Histograms of $\mathcal{R}$ (right panel) and S/N (middle panel) are shown, with the solid (blue) lines showing the predicted histogram given the most-likely estimates for S_0 and $n_{\rm ISS}$. The error bars show the standard Poisson uncertainties for each bin only. Bottom: rms residual $\sigma_{\mathcal{R}}$ in bins of S/N. The dashed line is the predicted TOA template-fitting error (not a fit to the points on the graph) based on the template shape while the solid line shows the estimated $\sigma_{\mathcal{R}}(S)$ from Equation (20) that includes a S/N-independent term.

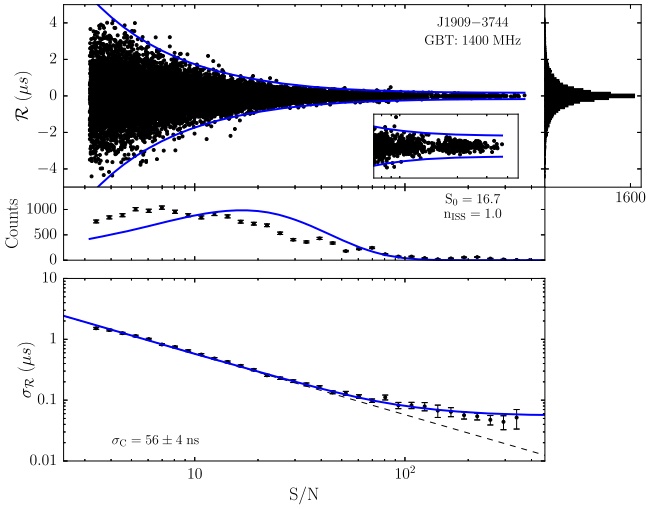

Figure 3. Analysis of residuals for PSR J1909−3744 observed at 1400 MHz with GBT. See the Figure 2 caption for more details.

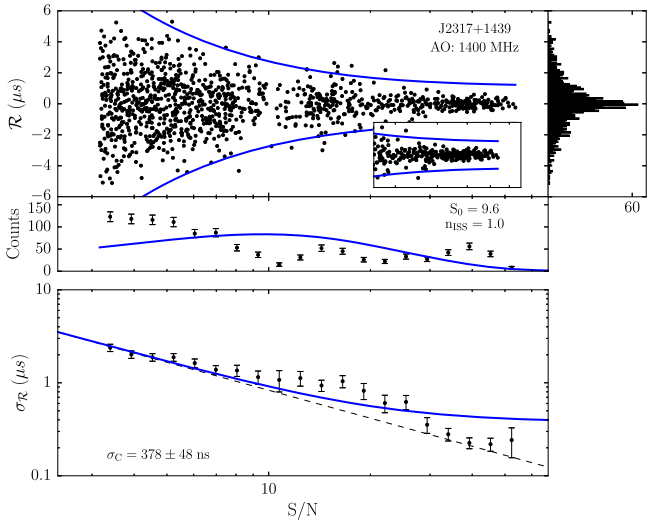

Figure 4. Analysis of residuals for PSR J2317+1439 observed at 1400 MHz with AO. See the Figure 2 caption for more details.

et al. 2016), of order the pulse channel bandwidth and typical total observation length. We see a similar result with PSR J2317+1439 though sparseness in the S/N histogram is a result of increased RFI excision for the pulsar. For PSR B1937+21, the S/N histogram is well described by the result of the ML analysis. The remaining low S/N residuals (S/N $\sim$ 10) are spurious noise spikes that pass our S/N cut criterion and lie close to the main pulse in phase. The narrowing of residuals at large S/N is not understood and may require further investigation of this pulsar. Lastly, we show the analysis for PSR J1918−0642 as a typical pulsar with an upper limit on σ_C.

To measure jitter values, we estimated $\sigma_{\rm DISS}$ as described in the previous section for 50 MHz sub-bands and subintegrations of length $t_{\rm sub}$ and then solved for σ_J given our measured σ_C (see

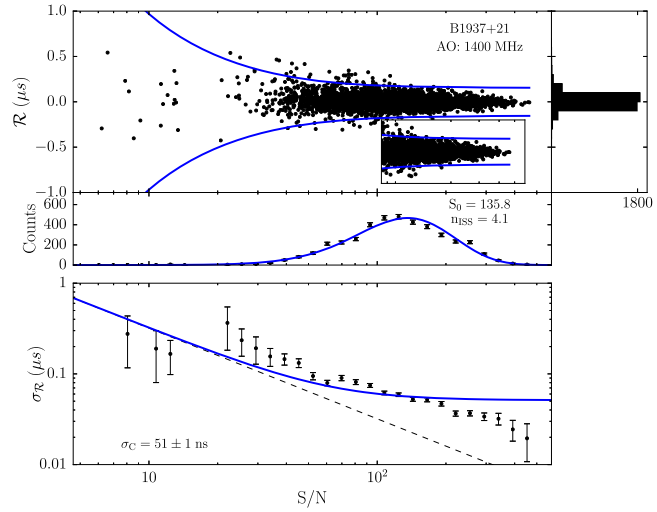

Figure 5. Analysis of residuals for PSR B1937+21 observed at 1400 MHz with AO. See the Figure 2 caption for more details.

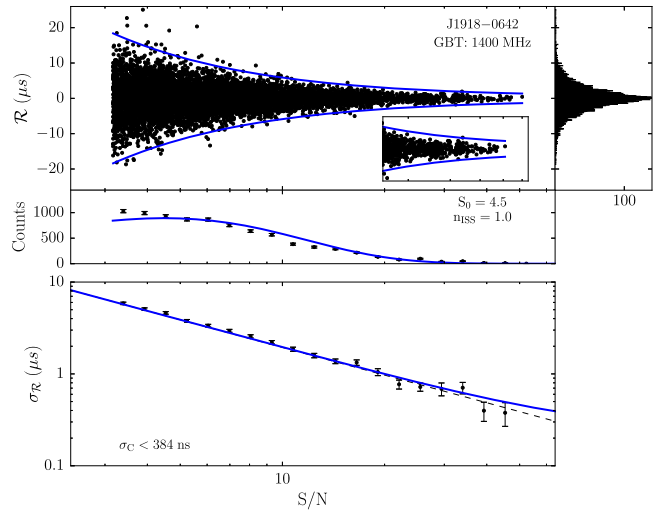

Figure 6. Analysis of residuals for PSR J1918−0642 observed at 1400 MHz with GBT. See the Figure 2 caption for more details. The 95% upper limit on σ_C is shown in the bottom left of the bottom panel, with the corresponding $\sigma_{\mathcal{R}}$ in blue.

Equation (20)). In several cases, the estimates of the scintillation noise from Equation (17) were larger than the σ_C estimated from the ML analysis, which is supposed to encapsulate all possible variance at high S/N. We employed a correlation analysis described in the next sub-section to separate the jitter and scintillation noise values for PSR B1937+21 at 1400 MHz, the only pulsar where the estimated σ_{DISS} is larger than σ_C and the S/N of the residuals is high enough to perform such an analysis.

4.3. Cross-correlation Analysis between Frequencies

Jitter causes simultaneously measured residuals at different frequencies to be correlated, which allows us to distinguish jitter noise from template-fitting noise. If the sub-band bandwidth is $\gtrsim \Delta\nu_d$, the residuals will not be correlated in frequency by DISS and we can distinguish jitter noise from scintillation noise as well. PSR B1937+21 has $\Delta\nu_d = 2.8 \pm 1.3$ MHz and $\Delta t_d = 327$ s at a reference frequency of 1500 MHz (Keith et al. 2013; Levin et al. 2016) and therefore residuals with 50 MHz of bandwidth will be correlated in frequency due to jitter only. We find $n_{ISS} \approx 4$ for PSR B1937+21 observed at 1400 MHz at AO with 50 MHz sub-bands and ∼80 s subintegrations. Therefore, the finite scintle effect is prominent and we expect scintillation noise to be large for this pulsar.

We let the total residual be the sum of the fluctuations from the three contributions to white noise,

$$\mathcal{R}(\nu, t) = \mathcal{R}_{S/N}(\nu, t) + \mathcal{R}_J(\nu, t) + \mathcal{R}_{DISS}(\nu, t), \quad (25)$$

where the subscripts denote the specific contribution. The cross-correlation coefficient between residuals from two sub-bands ν_i and ν_j is

$$\langle \mathcal{R}(\nu_i, t)\mathcal{R}(\nu_j, t)\rangle = \sigma_J^2, \quad (26)$$

where we assumed that the scintles are statistically independent between sub-bands for PSR B1937+21 and therefore do not correlate. The autocorrelation coefficient $\langle \mathcal{R}(\nu_i, t)^2\rangle$ reduces to the variance in Equation (1) plus cross terms that tend toward zero in the ensemble average limit. The correlation coefficient ρ is the autocorrelation coefficient divided by the square root of the cross-correlation coefficients between sub-bands, which we assumed to be identical within a single band. Therefore,

$$\rho(S) = \frac{\sigma_J^2}{\sigma_{\mathcal{R}}^2(S)} \quad (27)$$

and is a function of pulse S/N. Since we calculated ρ from residuals whose corresponding profiles differ in S/N, we took the average S/N for the profiles in a given sub-band and used the geometric mean $(\langle S_i\rangle\langle S_j\rangle)^{1/2}$ as a proxy for pulse S/N.

Figure 7 shows the correlation coefficients (gray) as a function of S, computed over all epochs observed at 1400 MHz for PSRs J1713+0747 (top) and B1937+21 (bottom) at AO (left) and GBT (right). Since PSR J1713+0747 has $\sigma_J \approx \sigma_C$ and high S/N, we show the results of our correlation analysis to demonstrate how the method performs before applying it to PSR B1937+21. The black points show the median ρ with linear bins in S/N each increasing by 10. The blue lines show the best fit of Equation (27) to the black points via a grid search in σ_J, holding $\sigma_{\mathcal{R}}$ fixed from the ML analysis. Each panel shows σ_J as a fraction of σ_C as well as the single-pulse rms $\sigma_{J,1}$, which accounts for the differences in t_{sub} between telescopes. The errors include both errors on σ_C and errors from the fit.

For PSR J1713+0747, we find consistency of $\sigma_{J,1}$ between AO and GBT, with $\sigma_{J,1} = 23.3 \pm 0.5$ μs, 22.5 ± 0.7 μs, respectively, which demonstrate a good check of the methods used in this paper. These values are generally consistent with, though somewhat lower than, measurements reported elsewhere. Dolch et al. (2014) report a measurement of jitter though their method includes the contribution from σ_{DISS}. They find $\sigma_{C,1} = 27.0 \pm 3.3$ μs, though we note that the σ_{DISS} contribution is not well-defined at the single-pulse level. Shannon & Cordes (2012) find $\sigma_{J,1} \approx 26$ μs from a cross-correlation analysis between frequency bands. Shannon et al. (2014) find $\sigma_{C,1} = 31.1 \pm 0.7$ μs (again including the contribution of σ_{DISS}) by adding Gaussian noise to the template, generating residuals, and subtracting the quadrature difference from the observed residuals. Even accounting for the small contribution from σ_{DISS}, their measurement formally disagrees with ours for reasons that are uncertain.

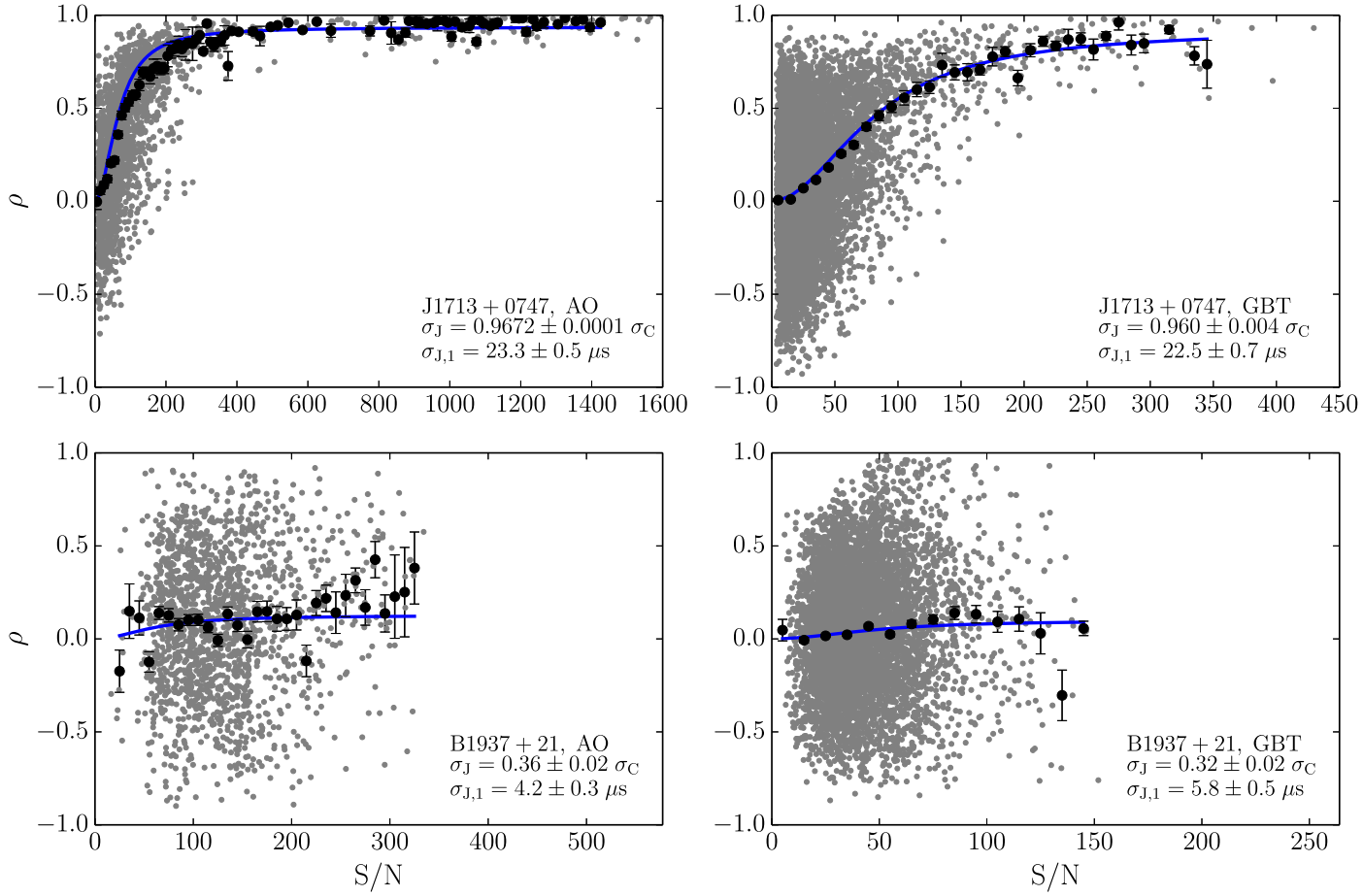

Figure 7. Correlation analysis for PSRs J1713+0747 (top) and B1937+21 (bottom) at AO (left) and GBT (right) for 1400 MHz band residuals. The gray points mark the correlation coefficient ρ of two different sub-bands of residuals on a given epoch as a function of the geometric average of the mean S/N of the pulse profiles for those sub-bands as $(\langle S_1\rangle\langle S_2\rangle)^{1/2}$. We show the median ρ in bins of S/N in black. The blue line marks the best-fit $\rho(S)$ to the black points.

For PSR B1937+21, $\sigma_{\rm DISS}$ is comparable to the predicted values from the scaling relation (Equation (17)) for both AO and GBT at 1400 MHz. Differences between the estimated $\sigma_{\rm J,1}$ between telescopes come from differences in the estimated $\sigma_{\rm C}$ whereas the ratio of RMSs $\sigma_{\rm J}/\sigma_{\rm C}$ is consistent between the measurements at both observatories. Since the GUPPI observations span more years than the PUPPI observations (∼3.6 years versus ∼1.6 years, respectively), if the scintillation parameters differed in the first half of the GUPPI observations than the second half when PUPPI ran in coincidence, then the average $\sigma_{\rm DISS}$ would differ between the two sets of observations. The small scintle size at 1400 MHz means that we are unable to study the scintillation properties of this pulsar with the current NANOGrav data set.

5. SUMMARY RESULTS

Figures 8 and 9 show the results for the three white-noise contributions to the timing residuals per frequency band per pulsar. We performed the ML analysis independently for observations of PSRs J1713+0747 and B1937+21, which were observed at both telescopes. For each frequency band, the pulsars are ordered in increasing amounts of template-fitting noise. Template-fitting noise values are calculated using Equation (5) and using the median and 68.3% confidence limits from the PDFs of S/N for each pulsar. Jitter values are also 68.3% confidence intervals or upper limits at the 95% level. DISS noise is calculated through scattering measurements as discussed in Section 3 and according to Equation (17). We scale the observation time T to 30 minutes and the bandwidth B equal to that of each receiver in NG9 (see Table 1 of Arzoumanian et al. 2015b).

To compare numbers expected over the length of a typical NANOGrav observation, we scaled all three contributions to 30 minutes. We multiplied the mean S/N, S_0 (see Equation (7)), by a factor of $\sqrt{30\ \text{minutes}/t_{\rm sub}}$, where $t_{\rm sub}$ is the subintegration time for either GBT (∼120 s) or AO, (∼80 s) to find the 30 minutes S/N for use in Equation (5). Because the scintillation timescales are of the order of the typical observation length or longer for most of these MSPs (Levin et al. 2016), the simple scaling relation of Equation (16) will hold on average though not exactly since the number of scintles in the time dimension is restricted. The scintillation noise term was scaled up in time and frequency using Equation (17). The gray band shows the template-fitting error scaled to the full bandwidth B by a factor of $\sqrt{50\ \text{MHz}/B}$. The rightmost panel shows the jitter parameter $k_{\rm J} = \sigma_{\rm J,1}/P$.

The raw values from our analysis are reported in Table 2. In Table 3, we convert all three white-noise contribution measurements to 30 minutes TOA uncertainties and rank the pulsars according to each contribution and to the total white noise per frequency band (thus matching Figures 8 and 9).

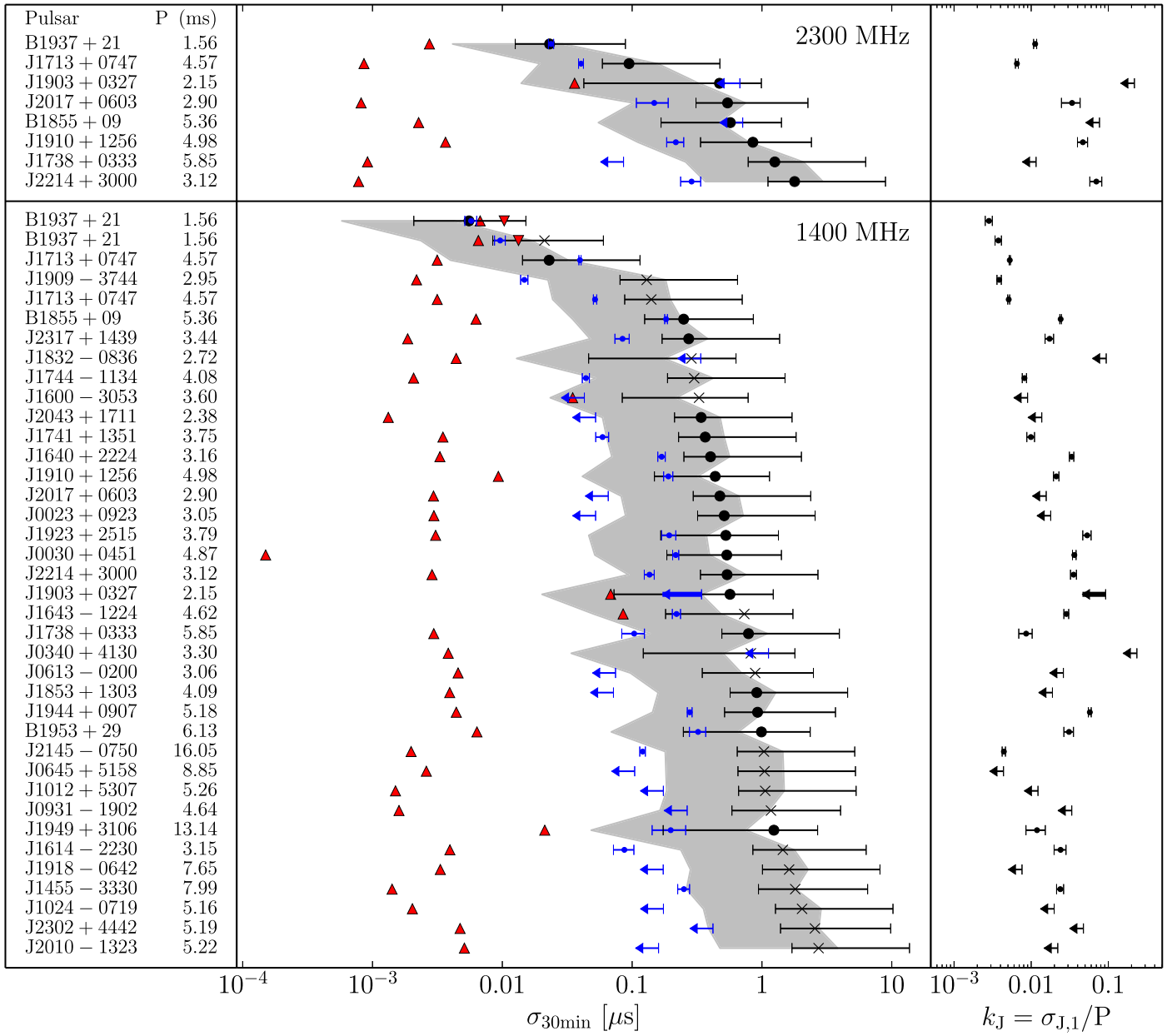

Figure 8. Summary of white-noise components for pulsars observed at the two highest frequency bands. The middle panel shows the three contributions, template-fitting noise as black circles (AO) or crosses (GBT), jitter noise as blue dots, and estimated DISS noise as red triangles. We observed PSRs J1713+0747 and B1937+21 with both telescopes and plot the separate analysis for each. The template-fitting and jitter contributions are for a 50 MHz bandwidth but scaled to a 30 minutes observating time. The gray bands represent the template-fitting noise scaled to the full receiver bandwidth to show the relative contribution with respect to jitter in a given NANOGrav observation. The DISS noise has been scaled to a 30 minutes observation and the appropriate total bandwidth for each band. Within each band, pulsars are ordered by increasing template-fitting noise (ordered by black points, not gray bands). The rightmost panel shows the single-pulse rms jitter divided by the period of the pulsar, k_J. For PSR B1937+21, the upside-down triangles indicate the measured DISS noise from the correlation analysis (see Section 4.3). The bold lines for PSR J1903+0327 at 1400 MHz indicates an upper limit on σ_C inconsistent with the estimate of σ_{DISS} (recall that σ_{DISS} has been scaled to the total bandwidth and a 30 minutes observing time and so appears smaller in the plot).

5.1. Pulse Jitter Statistics

The preceding analysis provides detections of σ_J for over half of the NANOGrav pulsars for the 1400 MHz band. This large sample allows us to examine the statistics of the jitter distribution. We use the jitter parameter k_J to compare pulsars, since it is independent of the pulse period.

Since $\sigma_{DISS} \ll \sigma_J$ for most pulsars in our sample at 1400 MHz, we can use the likelihood functions $\mathcal{L}(\sigma_C)$ computed in the ML analysis (see Equation (24)) as a proxy for the likelihood functions $\mathcal{L}(\sigma_J)$. In the case of PSR B1937+21, we explicitly set $\mathcal{L}(\sigma_J) = \mathcal{L}(\sqrt{\sigma_C^2 - \sigma_{DISS}^2})$. We ignore PSR J1903+0327 as the upper-limit $\mathcal{L}(\sigma_C)$ translates non-trivially to $\mathcal{L}(\sigma_J)$. We create a continuous histogram that is the sum of the individual likelihoods $\mathcal{L}(\sigma_J)$, shown in Figure 10. The black region shows the contributions from upper limit pulsar jitter values and the gray region shows the contributions from measured pulsar values. The median jitter parameter is $k_J = \sigma_J/P = 0.010^{+0.023}_{-0.006}$.

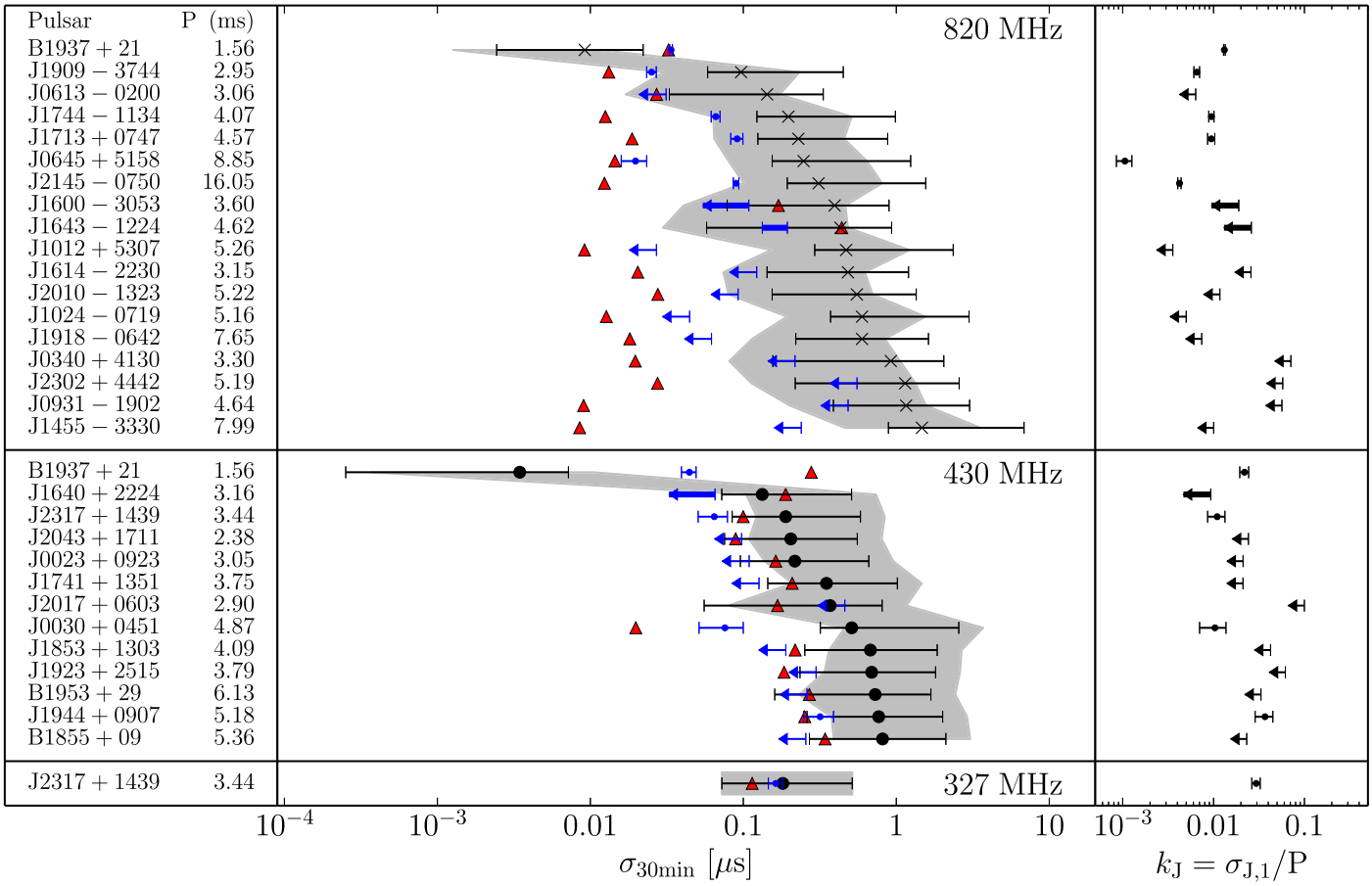

Figure 9. Summary of white-noise components for pulsars observed at the three lowest frequency bands. See the caption for Figure 8 for information. The bold upper limit lines for PSRs J1600−3053 and J1643−1224 at 820 MHz and J1640+2224 at 430 MHz, indicate an upper limit on σ_C inconsistent with the estimated σ_{DISS}.

6. NOISE MODEL AND IMPLICATIONS FOR PTA OPTIMIZATION

The noise covariance matrix for short timescales implied by our analysis is

$$\boldsymbol{C}_{\nu\nu',tt'} = \delta_{tt'}[\delta_{\nu\nu'}\sigma^2_{S/N}(S) + \sigma^2_J(T)] + \rho_{DISS,\nu\nu',tt'}\sigma^2_{DISS}(T), \quad (28)$$

where δ is the Kronecker delta and $\rho_{DISS,\nu\nu',tt'}$ encapsulates the correlation scales for DISS and we assume that bandwidth is fixed for each receiver. Shannon et al. (2014) find that jitter decorrelates over a range of frequencies larger than the total bandwidth of any receiver used in NG9; a decorrelation term is therefore not included in our model. We re-emphasize that $\sigma_{S/N}$ can be calculated directly from the template shape and σ_J is fixed for a given pulsar-frequency combination.

Pulsars dominated by template-fitting errors will see the greatest increase in timing precision from increased integration time and larger bandwidth instrumentation. Wideband timing systems allow for observations of an increased number of scintles and a reduction of σ_{DISS}. Therefore, higher DM pulsars, dominated by scintillation noise, will improve in timing quality and will would then become attractive candidates for inclusion into PTAs. By contrast, pulsars dominated by jitter on many epochs do not benefit substantially from wideband timing, though their timing precision will always improve with the increased numbers of pulses observed.

Scintillation monitoring is required in order to characterize the time-varying scintillation parameters, which will not only change σ_{DISS} but change the PBF over timescales much greater than that of a single epoch. Changes in the PBF will alter pulse shapes and therefore introduce a timing delay into any TOA estimate and contribute to the total white-noise variance.

NG9 uses an empirical, parameterized noise model fit in the timing analysis (Arzoumanian et al. 2015a, 2015b, 2015c). For TOAs with an associated error $\sigma_{S/N}$ from template-fitting, the white-noise model is

$$\boldsymbol{C}_{\nu\nu',tt'} = \delta_{tt'}[\delta_{\nu\nu'}(\mathcal{F}^2\sigma^2_{S/N}(S) + \mathcal{Q}^2) + \mathcal{J}^2], \quad (29)$$

where $\mathcal{F}$ (commonly referred to as EFAC) is a dimensionless, constant multiplier to the template-fitting error, $\mathcal{Q}$ (EQUAD) accounts for sources of Gaussian white noise added in quadrature to the template-fitting error, $\mathcal{J}$ (ECORR) accounts for sources of white noise correlated in frequency such as jitter. In NG9, $\mathcal{F} \approx 1$ for all pulsars, to within a factor of 2 for most pulsars. NG9 also fits a red noise model that is negligible on the timescales of a single epoch.

Figure 11 shows the comparison between measurements of $\mathcal{J}$ versus $\sigma_{J,30\,minutes}$ in black, with the gray points showing values where at least one of the two estimates is an upper limit. We find that $\sigma_{J,30\,minutes} \lesssim \mathcal{J}$, which suggests that ECORR is systematically measuring increases in the variance of the residuals, correlated in frequency, beyond pulse jitter. For example, broadband RFI can cause correlations in TOAs

Table 2
Maximum Likelihood Analysis Output

Pulsar	Period (ms)	DM (pc cm^{-3})	Telescope	Frequency (MHz)	$W_{\rm eff}$ (μs)	W_{50} (μs)	$t_{\rm sub}$[a] (s)	S_0	$n_{\rm ISS}$	$\sigma_{\rm C}$ (ns)	$+\sigma_{\sigma_{\rm C}}$ (ns)	$-\sigma_{\sigma_{\rm C}}$ (ns)
J0023+0923	3.05	14.33	AO	430	335	72	84.6	8.4	2.7	<363	…	…
			AO	1400	430	201	84.6	5.8	1.0	<273	…	…
J0030+0451	4.87	4.33	AO	430	705	643	85.9	9.6	1.0	380	120	122
			AO	1400	540	505	85.9	5.2	5.1	1328	71	71
J0340+4130	3.30	49.58	GBT	800	545	189	126.0	3.5	27.6	<999	…	…
			GBT	1400	515	213	126.0	3.7	37.0	<3301	…	…
J0613−0200	3.06	38.78	GBT	800	250	66	126.5	10.5	13.7	<97	…	…
			GBT	1400	331	274	126.5	2.4	3.7	<328	…	…
J0645+5158	8.85	18.25	GBT	800	590	70	128.8	20.3	1.0	85	16	16
			GBT	1400	627	117	128.8	5.1	1.0	<268	…	…
J0931−1902	4.64	41.49	GBT	800	669	296	126.5	3.6	5.5	<1323	…	…
			GBT	1400	466	348	126.5	2.8	1.9	<786	…	…
J1012+5307	5.26	9.02	GBT	800	667	691	128.8	12.1	1.0	<102	…	…
			GBT	1400	634	584	128.8	5.1	1.0	<343	…	…
J1024−0719	5.16	6.49	GBT	800	553	338	128.8	7.9	1.0	<138	…	…
			GBT	1400	574	141	128.8	2.4	1.0	<541	…	…
J1455−3330	7.99	13.57	GBT	800	956	440	121.7	5.2	1.1	<541	…	…
			GBT	1400	996	207	121.7	3.9	1.7	1542	162	161
J1600−3053	3.60	52.33	GBT	800	485	102	122.5	7.2	19.2	<277	…	…
			GBT	1400	424	70	122.5	7.7	10.6	<236	…	…
J1614−2230	3.15	34.50	GBT	800	449	109	122.5	5.6	7.5	<348	…	…
			GBT	1400	391	84	122.5	2.1	1.2	385	71	68
J1640+2224	3.16	18.43	AO	430	383	96	84.6	17.5	1.5	<135	…	…
			AO	1400	465	220	84.6	8.0	1.0	648	43	43
J1643−1224	4.62	62.41	GBT	800	1040	390	122.5	14.0	46.7	555	106	101
			GBT	1400	973	315	122.5	7.9	11.5	899	65	64
J1713+0747	4.57	15.99	AO	1400	539	110	82.0	159.9	1.0	180	4	3
			AO	2300	512	104	82.0	36.8	1.0	223	10	10
			GBT	800	694	170	121.7	22.1	1.5	268	24	24
			GBT	1400	533	109	121.7	31.4	1.0	143	4	4
J1738+0333	5.85	33.77	AO	1400	643	120	83.4	5.6	1.0	421	84	83
			AO	2300	696	118	83.4	3.8	1.0	<472	…	…
J1741+1351	3.75	24.19	AO	430	458	109	85.0	7.0	3.2	<475	…	…
			AO	1400	390	86	85.0	7.4	1.0	247	28	28
J1744−1134	4.07	3.14	GBT	800	513	147	121.7	21.6	1.0	225	15	15
			GBT	1400	511	137	121.7	14.1	1.0	193	12	12
			GBT	1400	187	49	121.7	3.8	30.6	<1006	…	…
J1853+1303	4.09	30.57	AO	430	486	606	83.4	3.7	4.2	<1035	…	…
			AO	1400	346	125	83.4	2.6	1.0	<451	…	…
B1855+09	5.36	13.30	AO	430	796	653	85.2	5.0	5.6	<888	…	…
			AO	1400	750	518	85.2	17.4	1.9	1025	25	25
			AO	2300	716	485	85.2	6.3	7.7	<2722	…	…
J1903+0327	2.15	297.54	AO	1400	405	195	82.6	3.4	51.3	<760	…	…
			AO	2300	327	99	82.6	3.3	108.8	<2023	…	…
J1909−3744	2.95	10.39	GBT	800	279	53	121.7	23.1	1.1	99	7	7
			GBT	1400	261	41	121.7	16.7	1.0	56	4	4
J1910+1256	4.98	38.06	AO	1400	634	133	82.0	7.3	5.3	823	67	67
			AO	2300	574	108	82.0	3.5	3.6	1819	273	273
J1918−0642	7.65	26.59	GBT	800	979	184	121.7	10.2	4.3	<377	…	…
			GBT	1400	879	151	121.7	4.5	1.0	<384	…	…
J1923+2515	3.79	18.86	AO	430	448	175	83.9	3.3	5.3	<1319	…	…
			AO	1400	534	146	83.9	5.1	6.4	1355	168	168
B1937+21	1.56	71.02	AO	430	190	63	84.1	263.1	170.5	448	48	50
			AO	1400	145	37	84.1	135.8	4.1	51	1	1
			AO	2300	147	36	84.1	38.4	1.5	76	4	4
			GBT	800	153	54	120.9	98.6	9.7	128	3	3
			GBT	1400	146	37	120.9	43.6	3.5	66	2	1
J1944+0907	5.18	24.34	AO	430	1120	500	83.4	7.4	5.3	1524	341	336
			AO	1400	949	364	83.4	6.3	1.4	2354	99	99
J1949+3106	13.14	164.13	AO	1400	916	142	80.8	3.5	41.8	1996	608	561
B1953+29	6.13	104.58	AO	430	1293	481	84.6	8.7	15.1	<1505	…	…
			AO	1400	823	224	84.6	4.1	11.2	1615	235	230
J2010−1323	5.22	22.16	GBT	800	499	240	121.7	5.4	8.6	<342	…	…

Table 2
(Continued)

Pulsar	Period (ms)	DM (pc cm^{-3})	Telescope	Frequency (MHz)	$W_{\rm eff}$ (μs)	W_{50} (μs)	$t_{\rm sub}$[a] (s)	S_0	$n_{\rm ISS}$	$\sigma_{\rm C}$ (ns)	$+\sigma_{\sigma_{\rm C}}$ (ns)	$-\sigma_{\sigma_{\rm C}}$ (ns)
			GBT	1400	527	247	121.7	1.6	1.0	<631	…	…
J2017+0603	2.90	23.92	AO	430	323	62	83.4	4.2	36.1	<1430	…	…
			AO	1400	242	64	83.4	3.5	1.0	<223	…	…
			AO	2300	234	61	83.4	2.7	1.3	578	162	157
J2043+1711	2.38	20.71	AO	430	222	35	83.5	5.6	4.3	<269	…	…
			AO	1400	178	21	83.5	3.6	1.0	<145	…	…
J2145−0750	16.05	9.01	GBT	800	1826	395	121.7	48.7	1.0	778	32	32
			GBT	1400	1823	339	121.7	14.6	1.0	815	40	40
J2214+3000	3.12	22.56	AO	1400	562	181	82.0	7.1	1.0	682	60	60
			AO	2300	551	180	82.0	2.1	1.0	1345	236	237
J2302+4442	5.19	13.76	GBT	800	608	345	128.8	3.2	20.9	<1588	…	…
			GBT	1400	682	347	128.8	2.0	1.5	<1307	…	…
J2317+1439	3.44	21.90	AO	327	395	152	85.7	11.6	3.5	677	71	72
			AO	430	392	169	85.7	11.4	2.6	266	58	57
			AO	1400	376	152	85.7	9.6	1.0	378	47	48

Note.
[a] Median subintegration length.

measured at different frequencies if unremoved. Replacement of the NG9 empirical white-noise model with our measurements will reduce the number of free parameters in the timing analysis and should improve overall sensitivity to GWs.

7. CONCLUSIONS

The short-term white-noise model for pulsar timing is well defined. We have estimated or placed limits on the contributions of the noise model's three white-noise components in the timing residuals of the NANOGrav PTA. The template-fitting errors are consistent with Equation (5) and dominate TOA precision for many of the pulsars for many epochs, but scintillation makes jitter important for the higher S/N epochs and TOAs. We find that the template-fitting and jitter errors can be estimated with only pulse S/N as a parameter. The total short-term variance needs contemporaneous measurements of scintillation parameters during observations to properly estimate the time-varying $\sigma_{\rm DISS}$ contribution. Errors in pulse polarization calibration, or those errors introduced from unremoved RFI, will produce extra variance on short timescales. Long-term observations spanning multiple epochs will have extra variance compared to the short-term model due to a variety of effects that are not included in our analysis.

A large subset of our observed pulsars are jitter-dominated on many epochs and we have measured jitter values for 22 of 37 pulsars. Major improvements in TOA estimation can therefore only be made through increased integration time. For several pulsars, however, $\sigma_{\rm DISS}$ is an important if not dominant contribution to the residuals. Wideband timing systems can yield improvements in pulsars with higher DMs such as PSRs B1937+21, J1600−3053, J1903+0327, and even moderate-DM pulsars like J2317+1439. Such systems can also improve the average S/N over all epochs, and therefore gains in timing precision can still be made for nearly all of the NANOGrav pulsars.

Jitter appears to be correlated in frequency over each band but not in time. We find that the rms phase variations from jitter are of order 1% of the pulse period, though with an extended tail toward higher values of the jitter parameter $k_{\rm J}$. Current noise models, such as the one used in NG9, utilize an empirical parameterization that overestimates the rms jitter. Replacement of model fit parameters with those that can be fixed will ultimately increase sensitivity of the PTA to GWs.

Future telescopes with increased collecting area and sensitivity will become jitter- and DISS-noise dominated. Arrays can therefore be partitioned and pointed at multiple pulsars simultaneously rather than one after another, providing longer integration times for each pulsar and increasing the number of pulses being averaged to reduce the jitter error contribution. The sub-arrays can be partitioned to minimize TOA uncertainty per target pulsar using the formalism outlined here. Wideband timing systems that allow for fine frequency- and time-resolution are needed to fully characterize scintillation structures on a per-epoch basis.

Author contributions. MTL developed the mathematical framework, created the modified data set and residuals, undertook the analysis, and prepared the majority of the text, figures, and tables. JMC and SC helped with the development of the framework, the format of figures and tables, and generated some additional text. JAE, DRM, and XS contributed useful discussions regarding the development of the framework. PBD assisted in the initial creation of the modified data set. ZA, KC, PBD, TD, RDF, EF, MEG, GJ, MJ, MTL, LL, MAM, DJN, TTP, SMR, IHS, KS, JKS, and WWZ all ran observations and developed timing models for the NG9 data set. Additional specific contributions are described in Arzoumanian et al. (2015b). JAE developed the noise model in NG9 and assisted in the comparison analysis to this work. JMC, SC, GJ, and DJN helped with review of the manuscript.

We would like to thank Michael Jones for useful discussions on statistical methods. The NANOGrav Project receives support from NSF PIRE program award number 0968296 and NSF Physics Frontier Center award number 1430284. NANOGrav research at UBC is supported by an NSERC Discovery Grant and Discovery Accelerator Supplement and the Canadian Institute for Advanced Research. MTL acknowledges partial support by NASA New York Space Grant award number NNX15AK07H. JAE acknowledges support by NASA through Einstein Fellowship grant PF3-140116. Portions of this

Table 3
Summary of White Noise Contributions Scaled to 30 Minutes

Pulsar	Period (ms)	DM (pc cm^{-3})	Telescope	$\sigma_{S/N}$ (ns)	σ_J (ns)	σ_{DISS} (ns)	$\sigma_{\mathcal{R}}$ (ns)	Rank S/N	Rank J	Rank DISS	Rank Total
					327 MHz						
J2317+1439	3.44	21.90	AO	181	163	114	269	1	1	1	1
					430 MHz						
J0023+0923	3.05	14.33	AO	313	<90	163	<364	5	6	4	5
J0030+0451	4.87	4.33	AO	737	75	19	742	8	4	1	8
J1640+2224	3.16	18.43	AO	191	49[a]	189	198[a]	2	2	7	1
J1741+1351	3.75	24.19	AO	504	<105	208	<556	6	7	8	6
J1853+1303	4.09	30.57	AO	977	<158	218	<1014	9	8	9	9
B1855+09	5.36	13.30	AO	1173	<213	342	<1240	13	9	13	13
J1923+2515	3.79	18.86	AO	996	<249	184	<1043	10	11	6	10
B1937+21	1.56	71.02	AO	5.0	44	278	281	1	1	12	2
J1944+0907	5.18	24.34	AO	1108	317	252	1179	12	12	10	12
B1953+29	6.13	104.58	AO	1051	<217	270	<1106	11	10	11	11
J2017+0603	2.90	23.92	AO	533	<384	167	<678	7	13	5	7
J2043+1711	2.38	20.71	AO	295	<81	89	<318	4	5	2	4
J2317+1439	3.44	21.90	AO	273	64	99	298	3	3	3	3
					820 MHz						
J0340+4130	3.30	49.58	GBT	478	<181	19	<511	15	15	11	15
J0613−0200	3.06	38.78	GBT	74	<26	27	<83	3	4	13	3
J0645+5158	8.85	18.25	GBT	128	19	14	130	6	1	8	5
J0931−1902	4.64	41.49	GBT	600	<403	9.0	<723	17	17	2	16
J1012+5307	5.26	9.02	GBT	243	<22	9.2	<244	10	2	3	9
J1024−0719	5.16	6.49	GBT	309	<37	12	<311	13	6	6	13
J1455−3330	7.99	13.57	GBT	762	<199	8.5	<788	18	16	1	18
J1600−3053	3.60	52.33	GBT	204	<81[a]	169	<220[a]	8	10	17	8
J1614−2230	3.15	34.50	GBT	250	<101	20	<271	11	13	12	10
J1643−1224	4.62	62.41	GBT	223	162[a]	440	276[a]	9	14	18	11
J1713+0747	4.57	15.99	GBT	118	91	18	150	5	12	10	6
J1744−1134	4.07	3.14	GBT	102	66	12	122	4	8	5	4
J1909−3744	2.95	10.39	GBT	50	25	13	57	2	3	7	2
J1918−0642	7.65	26.59	GBT	309	<51	18	<314	14	7	9	14
B1937+21	1.56	71.02	GBT	4.8	33	32	47	1	5	16	1
J2010−1323	5.22	22.16	GBT	286	<77	27	<297	12	9	15	12
J2145−0750	16.05	9.01	GBT	161	89	12	184	7	11	4	7
J2302+4442	5.19	13.76	GBT	591	<461	27	<750	16	18	14	17
					1400 MHz						
J0023+0923	3.05	14.33	AO	142	<43	3.0	<149	16	6	15	12
J0030+0451	4.87	4.33	AO	149	216	0.2	263	18	29	1	21
J0340+4130	3.30	49.58	GBT	229	<935	3.8	<963	23	38	22	38
J0613−0200	3.06	38.78	GBT	247	<62	4.6	<255	24	13	27	19
J0645+5158	8.85	18.25	GBT	292	<87	2.6	<305	29	16	11	24
J0931−1902	4.64	41.49	GBT	327	<221	1.6	<394	31	31	5	29
J1012+5307	5.26	9.02	GBT	295	<145	1.5	<329	30	22	4	27
J1024−0719	5.16	6.49	GBT	568	<145	2.0	<587	36	23	8	35
J1455−3330	7.99	13.57	GBT	503	250	1.4	562	35	32	3	34
J1600−3053	3.60	52.33	GBT	91	<35	34	<104	10	4	36	7
J1614−2230	3.15	34.50	GBT	404	87	3.9	413	33	15	24	31
J1640+2224	3.16	18.43	AO	112	168	3.3	202	13	24	19	14
J1643−1224	4.62	62.41	GBT	204	219	85	311	21	30	38	25
J1713+0747	4.57	15.99	AO	6.4	39	3.2	40	3	5	17	4
			GBT	39	51	3.2	65	5	9	18	5
J1738+0333	5.85	33.77	AO	219	103	3.0	243	22	17	14	18
J1741+1351	3.75	24.19	AO	102	59	3.5	117	12	11	21	10
J1744−1134	4.08	3.14	GBT	83	44	2.1	94	9	8	9	6
J1832−0836	2.72	28.18	GBT	79	<281	4.4	<292	8	35	25	22
J1853+1303	4.09	30.57	AO	254	<59	3.9	<261	25	12	23	20
B1855+09	5.36	13.30	AO	69	182	6.3	195	6	25	30	13
J1903+0327	2.15	297.54	AO	158	257[a]	68	301[a]	20	33	37	23

Table 3
(Continued)

Pulsar	Period (ms)	DM (pc cm^{-3})	Telescope	$\sigma_{S/N}$ (ns)	σ_J (ns)	σ_{DISS} (ns)	σ_R (ns)	Rank S/N	Rank J	Rank DISS	Rank Total
J1909−3744	2.95	10.39	GBT	36	14	2.2	39	4	3	10	3
J1910+1256	4.98	38.06	AO	121	190	9.3	226	14	26	32	16
J1918−0642	7.65	26.59	GBT	451	<144	3.3	<474	34	21	20	33
J1923+2515	3.79	18.86	AO	147	193	3.1	242	17	27	16	17
B1937+21	1.56	71.02	AO	1.6	5.7	10	11	1	1	33	1
			GBT	5.9	9.6	13	17	2	2	34	2
J1944+0907	5.18	24.34	AO	258	277	4.4	379	26	34	26	28
J1949+3106	13.14	164.13	AO	344	198	21	398	32	28	35	30
B1953+29	6.13	104.58	AO	276	321	6.4	424	27	36	31	32
J2010−1323	5.22	22.16	GBT	762	<133	5.1	<773	38	19	29	36
J2017+0603	2.90	23.92	AO	132	<54	3.0	<143	15	10	13	11
J2043+1711	2.38	20.71	AO	94	<43	1.3	<104	11	7	2	8
J2145−0750	16.05	9.01	GBT	288	120	2.0	312	28	18	7	26
J2214+3000	3.12	22.56	AO	150	136	2.9	202	19	20	12	15
J2302+4442	5.19	13.76	GBT	713	<349	4.7	<794	37	37	28	37
J2317+1439	3.44	21.90	AO	76	84	1.9	113	7	14	6	9
					2300 MHz						
J1713+0747	4.57	15.99	AO	31	40	0.9	51	2	2	3	2
J1738+0333	5.85	33.77	AO	414	<71	0.9	<420	7	3	4	5
B1855+09	5.36	13.30	AO	188	<592	2.3	<621	5	8	5	7
J1903+0327	2.15	297.54	AO	155	<563	36	<585	3	7	8	6
J1910+1256	4.98	38.06	AO	280	217	3.6	354	6	5	7	4
B1937+21	1.56	71.02	AO	7.6	23	2.7	25	1	1	6	1
J2017+0603	2.90	23.92	AO	179	148	0.8	232	4	4	2	3
J2214+3000	3.12	22.56	AO	588	287	0.8	654	8	6	1	8

Note.
[a] When the estimated σ_{DISS} is larger than the measured σ_C, entries for σ_J are replaced by the values for σ_C. The total residual rms σ_R is set equal to $\sqrt{\sigma_C^2 + \sigma_{S/N}^2}$.

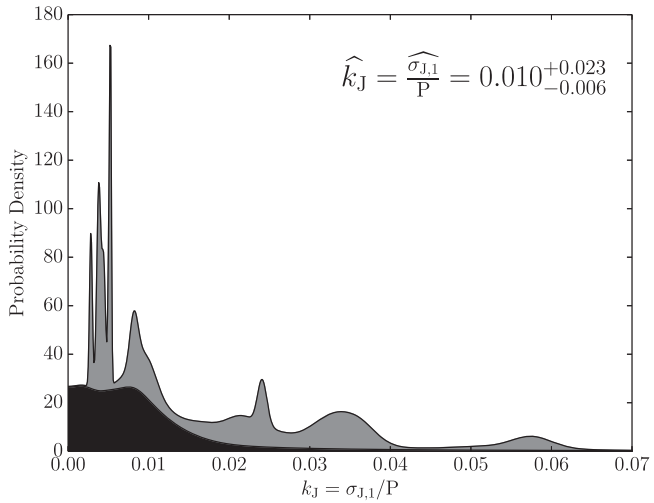

Figure 10. Continuous histogram of the jitter parameter $k_J = \sigma_{J,1}/P$. The shaded regions denote the probability density associated with measured values (gray) and upper limits (black) of k_J.

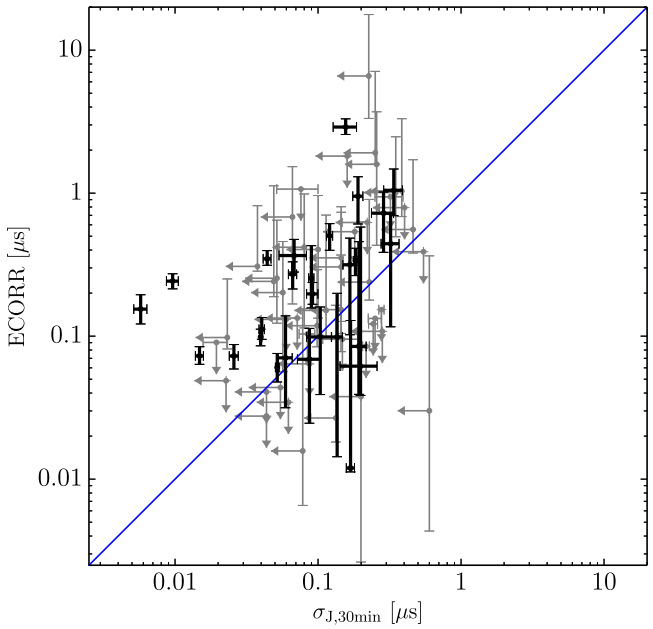

Figure 11. Comparison of ECORR from NG9 with jitter values from this work. Black points denote measurements in both while the gray points mark upper limits in at least one of the values for a given pulsar/receiver combination. The diagonal blue line shows where ECORR equals $\sigma_{J,30\ minutes}$.

research were carried out at the Jet Propulsion Laboratory, California Institute of Technology, under a contract with the National Aeronautics and Space Administration. TTP was a student at the National Radio Astronomy Observatory (NRAO) while this project was undertaken. Data for the project were collected using the facilities of the NRAO and the Arecibo Observatory. The NRAO is a facility of the NSF operated under cooperative agreement by Associated Universities, Inc. The Arecibo Observatory is operated by SRI International under a cooperative agreement with the NSF (AST-1100968), and in alliance with the Ana G. Méndez-Universidad

Metropolitana, and the Universities Space Research Association.

APPENDIX A
DEVIATIONS FROM THE INITIAL TIMING MODEL

Errors in the initial timing model parameters used for pulse folding and de-dispersion cause effects that can be separated into two related categories: an increase in TOA uncertainties from pulse shape changes on the subintegration timescale $t_{\rm sub}$, and correlated TOA errors over the observation duration T. The quadratic fit of initial timing residuals in Equation (19) will remove the latter, whereas the former cannot be mitigated after data collection. In part A.1 we discuss the non-removable pulse shape changes, in part A.2 we discuss the systematic deviations from the initial timing residuals that we remove with our quadratic fit, and in part A.3 we discuss other miscellaneous effects that can cause departures from the initial timing model.

A.1. Irreversible Pulse Profile Smearing

A.1.1. Spin Period Errors

If the initial folding period is incorrect by an amount δP, pulse profiles will be smeared by an amount

$$\sigma_P \sim \frac{\delta P}{P} t_{\rm sub}. \tag{30}$$

For isolated pulsars, the dominant folding error is due to an error in spin period,

$$\sigma_P \sim 10\ {\rm ps} \left(\frac{\delta P}{10^{-16}\ {\rm s}}\right) t_{100\ {\rm s}} P_{\rm ms}^{-1}, \tag{31}$$

where the typical error in the initial folding period is 10^{-16} s for pulsars in the NANOGrav data set. Note that periods fit over many years of data are known to much higher precision.

A.1.2. Binary Orbit Parameter Errors

For binary pulsars, the observed pulse period for low-eccentricity MSPs is Doppler-shifted by an amount (Lorimer & Kramer 2012)

$$\sigma_{P_b} \sim P \frac{\delta v_\parallel}{c} \sim \frac{2\pi P}{c} \delta\left(\frac{a \sin i}{P_b}\right)$$
$$\sim \frac{2\pi P a \sin i}{c P_b} \sqrt{\left(\frac{\delta a}{a}\right)^2 + \left(\frac{\delta(\sin i)}{\sin i}\right)^2 + \left(\frac{\delta P_b}{P_b}\right)^2} \tag{32}$$

$$\sim 72.7\ {\rm ns}\ \ P_{\rm ms}\ \ a_{\rm lsec}\ \ \sin i\ \ P_{b,{\rm day}}^{-1}$$
$$\times \sqrt{\left(\frac{\delta a}{a}\right)^2 + \left(\frac{\delta(\sin i)}{\sin i}\right)^2 + \left(\frac{\delta P_b}{P_b}\right)^2} \tag{33}$$

where a is the semimajor axis, i is the inclination angle, and P_b is the binary orbital period, and we assume that the errors in the binary parameters are uncorrelated. The error on these three parameters is much larger than the spin period error, with $\delta(\sin i)/\sin i \sim 10^{-3}$ dominating the other two binary error terms in the NANOGrav initial timing models even when $\sin i$ is well-measured. Therefore, for typical pulsar parameters and when $\sin i$ is measurable, the profile smearing error will be comparable to the spin period error but still negligible. Otherwise, the timing error will be of the order of 10 s of nanoseconds.

A.1.3. DM Variations

Differences in the initial timing model DM from the actual DM will cause smearing of pulse profiles. The timing perturbation is roughly the error in the dispersive delay across a frequency channel (Cordes 2002):

$$\delta t_{\rm DM} \simeq 8.3\ \mu{\rm s}\ \delta{\rm DM}\ {\rm B}_{\rm MHz} \nu_{\rm GHz}^{-3}, \tag{34}$$

with δDM measured in units of pc cm^{-3}. The typical range in total DM variation in the NANOGrav data set is $\sim 10^{-3}$ pc cm^{-3}, which given a 50 MHz channel bandwidth and an observing frequency of 1 GHz, yields a timing perturbation of ~400 ns. A constant DM over the observation is removed by the term $K(\nu)$ in the timing model fit. Intra-observation DM variations are discussed later in A.2.2.

A.1.4. Polarization Calibration Errors

Incorrect gain calibration and summation of the polarization profiles into the intensity profiles will cause pulse shape changes that lead to TOA uncertainties when fitting with a template. The TOA error from gain variation for circularly polarized channels is (Cordes et al. 2004)

$$\delta t_{\rm pol} \sim 1\ \mu{\rm s}\ \varepsilon_{0.1} \pi_{{\rm V},0.1} W_{0.1{\rm ms}}, \tag{35}$$

where $\varepsilon = \delta g/g$ is the fractional gain error, $\pi_{\rm V}$ is the degree of circular polarization, and W is the pulse width. Timing offsets from gain calibration errors will vary slowly with time and will be removed by the quadratic fit discussed in the next subsection (see for example A.2.3).

A.2. Systematic Deviations from the Quadratic Fit of Initial Timing Perturbations

A.2.1. Binary Orbit Parameter Errors

For pulsars in short-period binary orbits, we will need to fit out higher order terms in t when the period is of order the integration time over the epoch and the binary parameter errors are large. The shortest period binary in NG9 is PSR J0023+0923 with a period of 200 minutes, nearly seven times longer than the typical total integration time per epoch. The quadratic fit in Equation (19) will approximate the sinusoidal variations in TOA offsets introduced by the orbit mis-estimation. The next dominant polynomial term is the cubic term, with error $\sim \sigma_{P_b} (T/P_b)^3$, where $(T/P_b)^3 \sim 0.15^3 \sim 3.4 \times 10^{-3}$ for PSR J0023+0923 and smaller for all other pulsars in the NANOGrav data set. Therefore, using Equation (33), the error is negligible.

A.2.2. Ionospheric DM Variations

Changes in DM over short timescales, such as from ionospheric variations, will cause $K(\nu)$ to have time-dependence. The ionospheric DM will vary over the time span of a day due to the changing incident solar flux on a position on the Earth's surface by an amount $\lesssim 3 \times 10^{-5}$ pc cm^{-3} (Lam et al. 2015). The timing error is approximately the error in the dispersive delay across a frequency channel, given by Equation (34). For a maximum change in DM of 3×10^{-5} pc cm^{-3} over a 12 hr period, a 1 hr observing length, a 50 MHz

channel bandwidth, and an observing frequency of 1 GHz, the timing perturbation is ≈1 ns. Therefore, over the observing span, the assumption that $K(\nu, t) \approx K(\nu)$ holds.

A.2.3. Cross-coupling Errors

Instrumental self-polarization will cause a slow, secular variation in the initial timing residuals when unremoved (Cordes et al. 2004). Cross coupling in the feed will induce a measured false circular polarization $\pi_V \simeq 2\eta^{1/2}\pi_L$, where η is the voltage cross coupling coefficient and π_L is a pulsar's degree of linear polarization. While the associated timing errors can be large, errors introduced by the cross-coupling term will cause a slow, secular variation in the residuals as the feed rotates during an observation and will therefore be removed by our quadratic fit. Estimates of these parameters and the induced timing uncertainties will be focused on in future papers.

A.2.4. Rotation Measure (RM) Variations

Faraday rotation from magnetic fields along the pulse propagation path causes both a birefringent TOA delay and the pulse polarization position angle (PPA) to rotate. Changes in the rotation measure ($\mathrm{RM} = \int dl\, n_e B_\parallel$, in units of rad m^{-2}) over short timescales can come from ionospheric variations as with DM. The birefringent delay is given as (Cordes 2002)

$$\delta t_{\mathrm{RM}} = 0.18 \text{ ns RM } \nu_{\mathrm{GHz}}^{-3} \tag{36}$$

and the change in PPA is (Lorimer & Kramer 2012)

$$\Delta\Psi_{\mathrm{PPA}} = \mathrm{RM}\, \lambda^2 = 0.09 \text{ RM } \nu_{\mathrm{GHz}}^{-2}. \tag{37}$$

The RM through the ionosphere is ∼1 rad m^{-2} with ∼10% variations on the timescale of 1 hr (Sotomayor-Beltran et al. 2013) and the birefringent delay is therefore negligible over short timescales. The change in the PPA will cause errors in the polarization calibration that are slowly varying with time and therefore removed by the quadratic fit.

A.2.5. Intrinsic Pulsar Spin Noise

Rotational instabilities in the pulsar cause deviations from the initial timing model with a steep, power-law noise spectrum over the timescale of years (Cordes 2013). Shannon & Cordes (2010) measured spin noise in radio pulsars to scale as $\sigma_{\mathrm{spin}} \propto T^{2.0\pm0.2}$. The pulsar with the largest measured rms spin noise in the NANOGrav data set is PSR B1937+21, with $\sigma_{\mathrm{spin}} \approx 1.5\ \mu$s over 10 years (Shannon & Cordes 2010; Arzoumanian et al. 2015b). The rms on the timescale of 1 hr is ∼0.2 fs and is therefore negligible.

A.2.6. Stochastic GW Background

Like intrinsic pulsar spin noise, GW perturbations will also induce long-term correlations in residuals. However, the rms timing perturbation from a stochastic GW background of supermassive black hole binaries over 10 years is on the order of 100 ns (Siemens 2013). The rms is expected to scale as $\sigma_{\mathrm{GW}} \propto T^{5/3}$, and therefore on the timescale of 1 hr the rms is ∼0.6 fs and is also negligible.

A.3. Increases in Variance from Other Effects

A.3.1. Frequency-dependent DM

Cordes et al. (2016) describe differences in DM measured at different frequencies due to multipath scattering in the ISM and different volumes of electrons probed. The different DMs as a function of frequency cause differences in the frequency-dependent delays per channel, $K(\nu)$. However, the timescales of refractive variations are weeks or longer, and therefore this effect is negligible on short timescales.

A.3.2. Mean PBF Variations

As with frequency-dependent DM, the changes in PBFs will occur on a pulsar's refractive timescale and will therefore be negligible on a timescale of an hour.

A.3.3. Pulsar Mode Changes

Any potential mode changes may cause timing parameter differences from the initial timing model. Pulse profile shapes in our MSPs have not been shown to deviate from the template over the timespan of single observations and any possible epoch-to-epoch mode changes are small and will be removed by our quadratic fit to obtain the short-term timing model (Equation (19)).

A.3.4. Transient Events

Giant pulses have been seen in pulsars such as PSR B1937+21 and cause pulse shapes to deviate from the average template shape (Cognard et al. 1996; Jenet et al. 2001; Zhuravlev et al. 2013). For PSR B1937+21, giant pulses will appear at a rate of approximately 0.5 per 10 s pulse average, which spans ≈6400 pulse periods. Therefore, the giant pulse S/N must be a factor of $\sim\sqrt{6400} \sim 80$ larger than the average single-pulse S/N in order to dominate the template matching fit and significantly alter the estimated TOA. The flux density of the strongest giant pulse in Zhuravlev et al. (2013) is a factor of ∼3 smaller than the threshold needed to affect the TOA estimation.

A.3.5. Remaining RFI

Any remaining RFI in the pulse profiles will introduce unmodeled variance into our analysis. Broadband RFI can cause correlations between residuals that can increase estimates of jitter.

APPENDIX B
PDF OF TOA ERRORS DUE TO COMBINED ADDITIVE NOISE AND ISS MODULATION

The template-fitting error (Equation (5)) can be written in the form

$$\sigma_{\mathrm{S/N}} = \sigma_0 \frac{S_0}{S}. \tag{38}$$

Again, S is the S/N, proportional to $(S_{\mathrm{PSR}}/\mathrm{SEFD})\sqrt{2BT}$, where S_{PSR} is the pulsar flux density, SEFD is the system equivalent flux density, B is the receiver bandwidth, and T is the total integration time. The subscript "0" is used to denote intrinsic values. We assume that S_0 is constant, meaning that

both the pulsar flux density and system parameters are also constant (see Section 4.2).

We describe changes in S_0 with a multiplicative gain factor g such that $S = gS_0$. The PDF of the scintillation gains due to DISS with $n_{\rm ISS}$ scintles contributing to the measured profile is given by a chi-squared distribution with $2n_{\rm ISS}$ degrees of freedom (Cordes & Chernoff 1997, Appendix B):

$$f_g(g|n_{\rm ISS}) = \frac{(gn_{\rm ISS})^{n_{\rm ISS}}}{g\Gamma(n_{\rm ISS})} e^{-gn_{\rm ISS}}\Theta(g). \quad (39)$$

Unlike DISS, gains from RISS will vary slowly with both time and frequency. For media that follow a Kolmogorov-type electron density wavenumber spectrum with small refractive modulations, DISS and RISS are decoupled in the strong scattering regime. RISS will have a symmetric PDF if focusing is not important and can be approximated with a Gaussian distribution, $f_{g_{\rm RISS}}(g) = \mathcal{N}(0, \sigma^2_{\rm RISS})$ with some correlation time much greater than the observing duration T (Stinebring et al. 2000). The total gain can be written $g = g_{\rm DISS}g_{\rm RISS}$.

We can solve for the PDF of scintillated pulse S/Ns under a change of variables. Equation (39) becomes

$$f_S(S|n_{\rm ISS}) = f_g(g|n_{\rm ISS})\frac{dg}{dS} \quad (40)$$

$$= f_g\left(\frac{S}{S_0}|n_{\rm ISS}\right)\frac{1}{S_0} \quad (41)$$

$$= \frac{(Sn_{\rm ISS}/S_0)^{n_{\rm ISS}}}{S\Gamma(n_{\rm ISS})} e^{-Sn_{\rm ISS}/S_0}\Theta(S). \quad (42)$$

We can also quantify the distribution of TOA errors, Δt, from scintillation. Errors solely from template fitting in the unscintillated case, Δt_0, will be normally distributed, written as

$$f_{\Delta t_0}(\Delta t_0) = \mathcal{N}(0, \sigma^2_{S_0}). \quad (43)$$

As in Equation (5), we rewrite the rms error is

$$\sigma_{\rm S/N} = \frac{W_{\rm eff}}{S\sqrt{N_\phi}} \quad (44)$$

$$= \frac{W_{\rm eff}}{gS_0\sqrt{N_\phi}} \quad (45)$$

$$= \frac{\sigma_{S_0}}{g}. \quad (46)$$

Again, under a change of variables, we can write

$$f_{\Delta t}(\Delta t|g) = f_{\Delta t_0}(\Delta t_0)\frac{d\Delta t_0}{d\Delta t} \quad (47)$$

$$= gf_{\Delta t_0}(g\Delta t). \quad (48)$$

For brevity, we will write $Z = |\Delta t|/\sigma_{\Delta t_0}$. The marginal PDF is then

$$f_{\Delta t}(\Delta t) = \int_{-\infty}^{\infty} dg\, f_g(g) f_{\Delta t}(\Delta t|g) \quad (49)$$

$$= \int_{-\infty}^{\infty} dg\, g\, f_g(g) f_{\Delta t_0}(g\Delta t_0) \quad (50)$$

$$= \int_{-\infty}^{\infty} dg\, g\, e^{-g}\,\Theta(g)\,\frac{1}{\sigma_{S_0}\sqrt{2\pi}}\exp\left(-\tfrac{1}{2}Z^2\, g^2\right) \quad (51)$$

$$= \frac{1}{\sigma_{S_0}\sqrt{2\pi}}\int_0^{\infty} dg\, g\, e^{-g}\exp\left(-\tfrac{1}{2}Z^2\, g^2\right). \quad (52)$$

From Gradshteyn et al. (2007), Equation (3.462.1), we have

$$\int_0^{\infty} x^{\alpha-1}e^{-\beta x^2-\gamma x}dx = (2\beta)^{-\alpha/2}\Gamma(\alpha)e^{\gamma^2/(8\beta)} \times D_{-\alpha}\left(\frac{\gamma}{\sqrt{2\beta}}\right),\ \mathrm{Re}\,\beta > 0,\ \mathrm{Re}\,\alpha > 0, \quad (53)$$

where $D_n(x) = 2^{-n/2}e^{-x^2/4}H_n(x/\sqrt{2})$ is the parabolic cylinder function defined in terms of the Hermite polynomial of order n, $H_n(x)$. For this calculation, we have $\alpha = n_{\rm ISS} + 1$, $\beta = \frac{1}{2}Z^2$, $\gamma = n_{\rm ISS}$. Thus, we can write

$$f_{\Delta t}(\Delta t|n_{\rm ISS}) = \frac{1}{\sigma_{S_0}\sqrt{2\pi}}\frac{n_{\rm ISS}^{n_{\rm ISS}}}{\Gamma(n_{\rm ISS})}Z^{-(n_{\rm ISS}+1)}\Gamma(n_{\rm ISS}+1) \times \exp\left(\frac{n_{\rm ISS}^2}{4Z^2}\right)D_{-(n_{\rm ISS}+1)}\left(\frac{n_{\rm ISS}}{Z}\right) \quad (54)$$

$$= \frac{1}{\sigma_{S_0}\sqrt{2\pi}}\left(\frac{n_{\rm ISS}}{Z}\right)^{n_{\rm ISS}+1} \times \exp\left(\frac{1}{4}\left(\frac{n_{\rm ISS}}{Z}\right)^2\right)D_{-(n_{\rm ISS}+1)}\left(\frac{n_{\rm ISS}}{Z}\right) \quad (55)$$

$$= \frac{1}{\sigma_{S_0}\sqrt{2\pi}}\left(\frac{\sqrt{2}n_{\rm ISS}}{Z}\right)^{n_{\rm ISS}+1}H_{-(n_{\rm ISS}+1)}\left(\frac{n_{\rm ISS}}{\sqrt{2}Z}\right). \quad (56)$$

In the case where $n_{\rm ISS} = 1$, this reduces to

$$f_{\Delta t}(\Delta t|n_{\rm ISS}) = \frac{1}{\sigma_{S_0}\sqrt{2\pi}}\left(Z^2 - \frac{\sqrt{\pi}\exp\left(\frac{1}{2Z^2}\right)\mathrm{erfc}\left(\frac{1}{\sqrt{2}Z}\right)}{\sqrt{2}Z^3}\right). \quad (57)$$

REFERENCES

Antoniadis, J. I. 2013, Ph.D. thesis, Univ. Bonn
Armstrong, J. W. 1984, Natur, 307, 527
Arzoumanian, Z., Brazier, A., Burke-Spolaor, S., et al. 2015a, ApJ, 810, 150
Arzoumanian, Z., Brazier, A., Burke-Spolaor, S., et al. 2015b, ApJ, 813, 65
Arzoumanian, Z., Brazier, A., Burke-Spolaor, S., et al. 2015c, arXiv:1508.03024
Backer, D. C., Rankin, J. M., & Campbell, D. B. 1975, ApJ, 197, 481
Blandford, R., Romani, R. W., & Narayan, R. 1984, JApA, 5, 369
Cognard, I., Shrauner, J. A., Taylor, J. H., & Thorsett, S. E. 1996, ApJL, 457, L81
Coles, W. A., Kerr, M., Shannon, R. M., et al. 2015, ApJ, 808, 113
Cordes, J. M. 2002, in ASP Conf. Proc. 278, Single-Dish Radio Astronomy, Techniques and Applications, ed. S. Stanimirovic, D. Altschuler, P. Goldsmith, & C. Salter (San Francisco, CA: ASP), 227
Cordes, J. M. 2013, CQGra, 30, 224002
Cordes, J. M., & Chernoff, D. F. 1997, ApJ, 482, 971
Cordes, J. M., & Downs, G. S. 1985, ApJS, 59, 343
Cordes, J. M., Kramer, M., Lazio, T. J. W., et al. 2004, NewAR, 48, 1413
Cordes, J. M., & Lazio, T. J. W. 2002, arXiv:astro-ph/0207156
Cordes, J. M., & Rickett, B. J. 1998, ApJ, 507, 846
Cordes, J. M., & Shannon, R. M. 2010, arXiv:1010.3785
Cordes, J. M., Shannon, R. M., & Stinebring, D. R. 2016, ApJ, 817, 16
Cordes, J. M., Wolszczan, A., Dewey, R. J., Blaskiewicz, M., & Stinebring, D. R. 1990, ApJ, 349, 245
Craft, H. D., Jr. 1970, Ph.D. thesis, Cornell Univ.
Demorest, P. B. 2007, Ph.D. thesis, Univ. California
Demorest, P. B., Ferdman, R. D., Gonzalez, M. E., et al. 2013, ApJ, 762, 94

Demorest, P. B., Pennucci, T., Ransom, S. M., Roberts, M. S. E., & Hessels, J. W. T. 2010, Natur, 467, 1081
Dolch, T., Lam, M. T., Cordes, J., et al. 2014, ApJ, 794, 21
DuPlain, R., Ransom, S., Demorest, P., et al. 2008, Proc. SPIE, 7019, 70191D
Ford, J. M., Demorest, P., & Ransom, S. 2010, Proc. SPIE, 7740, 77400A
Foster, R. S., & Cordes, J. M. 1990, ApJ, 364, 123
Gradshteyn, I. S., Ryzhik, I. M., Jeffrey, A., & Zwillinger, D. 2007, in Table of Integrals, Series, and Products, ed. I. S. Gradshteyn et al. (7th ed.; Amsterdam: Elsevier), 2007
Hassall, T. E., Stappers, B. W., Hessels, J. W. T., et al. 2012, A&A, 543, A66
Hobbs, G., Lyne, A. G., & Kramer, M. 2010, MNRAS, 402, 1027
Hotan, A. W., van Straten, W., & Manchester, R. N. 2004, PASA, 21, 302
Jenet, F. A., Anderson, S. B., & Prince, T. A. 2001, ApJ, 546, 394
Keith, M. J., Coles, W., Shannon, R. M., et al. 2013, MNRAS, 429, 2161
Kramer, M. 1998, ApJ, 509, 856
Kramer, M., Xilouris, K. M., Lorimer, D. R., et al. 1998, ApJ, 501, 270
Lam, M. T., Cordes, J. M., Chatterjee, S., et al. 2015, arXiv:1512.02203
Lambert, H. C., & Rickett, B. J. 1999, ApJ, 517, 299
Lazaridis, K., Wex, N., Jessner, A., et al. 2009, MNRAS, 400, 805
Lentati, L., Hobson, M. P., & Alexander, P. 2014, MNRAS, 444, 3863
Levin, L., McLaughlin, M. A., Jones, G., et al. 2016, arXiv:1601.04490
Liu, K., Keane, E. F., Lee, K. J., et al. 2012, MNRAS, 420, 361
Liu, K., Verbiest, J. P. W., Kramer, M., et al. 2011, MNRAS, 417, 2916
Lorimer, D. R., & Kramer, M 2012, in Handbook of Pulsar Astronomy, ed. D. R. Lorimer, & M. Kramer (Cambridge: Cambridge Univ. Press), 2012
Lyne, A., Graham-Smith, F., Weltevrede, P., et al. 2013, Sci, 342, 598
McLaughlin, M. A. 2013, CQGra, 30, 224008
Pennucci, T. T., Demorest, P. B., & Ransom, S. M. 2014, ApJ, 790, 93
Perera, B. B. P., McLaughlin, M. A., Kramer, M., et al. 2010, ApJ, 721, 1193
Phillips, J. A., & Wolszczan, A. 1992, ApJ, 385, 273
Pilia, M., Hessels, J. W. T., Stappers, B. W., et al. 2016, A&A, 586, A92
Rickett, B. J. 1990, ARA&A, 28, 56
Shannon, R. M., & Cordes, J. M. 2010, ApJ, 725, 1607
Shannon, R. M., & Cordes, J. M. 2012, ApJ, 761, 64
Shannon, R. M., Osłowski, S., Dai, S., et al. 2014, MNRAS, 443, 1463
Shao, L., & Wex, N. 2013, CQGra, 30, 1650
Siemens, X. 2013, CQGra, 30, 224015
Sotomayor-Beltran, C., Sobey, C., Hessels, J. W. T., et al. 2013, A&A, 552, A58
Stinebring, D. R., Smirnova, T. V., Hankins, T. H., et al. 2000, ApJ, 539, 300
Taylor, J. H. 1992, RSPTA, 341, 117
Turin, G. L. 1960, IRE Trans. on Information Theory, IT-6, 3, 311
van Haasteren, R., Levin, Y., McDonald, P., & Lu, T. 2009, MNRAS, 395, 1005
van Straten, W., Demorest, P., & Oslowski, S. 2012, AR&T, 9, 237
Verbiest, J. P. W., Bailes, M., Coles, W. A., et al. 2009, MNRAS, 400, 951
Will, C. M. 2014, LRR, 17, 4
Yan, Z., Shen, Z.-Q., Wu, X.-J., et al. 2015, ApJ, 814, 5
Zhu, W. W., Stairs, I. H., Demorest, P. B., et al. 2015, ApJ, 809, 41
Zhuravlev, V. I., Popov, M. V., Soglasnov, V. A., et al. 2013, MNRAS, 430, 2815